Peer reviewed paper

Title: Liquid CO_2 injection for geological storage in deep saline aquifers

Authors: Víctor Vilarrasa, Orlando Silva, Jesús Carrera and Sebastià Olivella

Journal published: International Journal of Greenhouse Gas Control

Volume and pages: Vol. 14, pp. 84-96

Publication year: 2013

LIQUID CO_2 INJECTION FOR GEOLOGICAL STORAGE IN DEEP SALINE AQUIFERS

Víctor Vilarrasa[1,2], Orlando Silva[3], Jesús Carrera[1] and Sebastià Olivella[2]

[1] GHS, Institute of Environmental Assessment and Water Research (IDAEA), CSIC, Jordi Girona 18-26, 08034 Barcelona, Spain

[2] Dept Geotechnical Engineering and Geosciences, Technical University of Catalonia (UPC-BarcelonaTech), Jordi Girona 1-3, 08034 Barcelona, Spain

[3] Fundación Ciudad de la Energía (CIUDEN), CO_2 Geological Storage Programme, Av. Segunda nº 2 (Poblado de Compostilla), 24404 Ponferrada (León), Spain

ABSTRACT

CO_2 will remain in supercritical (SC) state (i.e. p>7.382 MPa and T>31.04 ºC) under the pressure (p) and temperature (T) conditions appropriate for geological storage. Thus, it is usually assumed that CO_2 will reach the aquifer in SC conditions. However, inflowing CO_2 does not need to be in thermal equilibrium with the aquifer. In fact, surface operations are simpler for liquid than for SC CO_2, because CO_2 is transported in liquid state. Yet, problems might arise because of thermal stresses induced by cold CO_2 injection and because of phase changes in the injection tubing or in the formation. Here, we propose liquid CO_2 injection and analyze its evolution and the thermo-hydro-mechanical response of the formation and the caprock. We find that injecting CO_2 in liquid state is energetically more efficient than in SC state because liquid CO_2 is denser than SC CO_2, leading to a lower overpressure not only at the wellhead, but also in the reservoir because a smaller fluid volume is displaced. Cold CO_2 injection cools down the formation around the injection well. Further away, CO_2 equilibrates thermally with the medium in an abrupt front. The liquid CO_2 region close to the injection well advances far behind the SC CO_2 interface. While the SC CO_2 region is dominated by gravity override, the liquid CO_2 region displays a steeper front because viscous forces dominate (liquid CO_2 is not only denser, but also more viscous than SC CO_2). The temperature decrease close to the injection well induces a stress reduction due to thermal contraction of the media. This can lead to shear slip of pre-existing fractures in the aquifer for large temperature contrasts in stiff rocks, which could enhance injectivity. In contrast, the mechanical stability of the caprock is improved in stress regimes where the maximum principal stress is the vertical.

Keywords: CO_2 density, energy efficiency, pressure buildup, thermo-mechanical effects, caprock mechanical stability.

1.- INTRODUCTION

Pressure (p) and temperature (T) conditions of deep geological formations suitable for storing carbon dioxide (CO_2) are such that this greenhouse gas remains in supercritical (SC) state, i.e. p>7.382 MPa and T>31.04 ºC (e.g. Bachu, 2003). Thus, it is usually assumed that CO_2 will reach the aquifer in SC conditions (e.g. Pruess and Garcia, 2002). However, injecting CO_2 in SC state may not be the best option. Several engineering methodologies have been proposed as alternatives to the concept of injecting SC CO_2. They focus on accelerating CO_2 dissolution to minimize the risk of leakage of free-phase mobile CO_2 by means of dissolving CO_2 at surface (Burton and Bryant, 2009; Jain and Bryant, 2011; Zendehboudi *et al*., 2011) or at depth (Carrera *et al*., 2011b), by injecting brine at some distance from the CO_2 injection well that mixes with the CO_2 plume enhancing dissolution (Hassanzadeh *et al*., 2009) or by injecting CO_2 under temporal pressure fluctuations, which enhances CO_2 dissolution (Bolster *et al*., 2009). On the other hand, a few studies suggest that cold CO_2 (and therefore in liquid state) injection may have some advantageous implications for CO_2 storage (Rayward-Smith and Woods, 2011; Silva *et al.*, 2011). However, these studies are approximations that do not take into account the whole coupling of the thermo-hydro-mechanical effects inherent to cold CO_2 injection.

It can be conjectured that injecting CO_2 in liquid state is energetically more efficient than doing so in SC state and more optimal from a storage engineering point of view

because liquid CO_2 is denser than SC CO_2. Therefore, for a given mass of CO_2, a smaller volume of formation fluid will be displaced, leading to a lower overpressure in the reservoir. More importantly, the increased weight of liquid CO_2 in the injection well implies that a far lower pressure is required at the wellhead. Additionally, CO_2 is usually transported in liquid state (pressure above 8.5 MPa and ambient temperatures (Figure 1)) (McCoy and Rubin, 2008). Thus, it can be injected at the conditions in which it arrives to the wellhead, without having to perform throttling or heating operations. In fact, since pressure at the wellhead is reduced, it may be smaller than transport pressure, which may allow recovering some energy from the incoming CO_2. Furthermore, if pressure needs to be increased, a smaller compression work has to be done to inject liquid CO_2 because liquid CO_2 is less compressible than SC CO_2. This compression can be performed by means of pumps without having to use compressors, which are much harder to operate. Despite these apparent advantages, liquid CO_2 injection has not been considered in the scientific literature and it has not been attempted in practice except for the case of Snøhvit, where CO_2 is injected in liquid state at the wellhead (at 4 ºC because the wellhead, placed on the seabed at 300 m below the sea surface, thermally equilibrates with the sea), but reaches the reservoir, placed at 2700 m below the seabed, in SC conditions because CO_2 thermally equilibrates with the geothermal gradient (at 98 ºC in the reservoir) (Estublier and Lackner, 2009). This may reflect the fact that so far industrial operations have been associated to oil industry, where CO_2 is obtained in gas form. It may also reflect fear to phase transitions in the injection equipment or in the formation, or to thermal (thermo-mechanical) stresses associated to a cold fluid injection.

Hydro-mechanical, but not thermo-mechanical, effects have been widely investigated in the context of geological storage of CO_2 (e.g. Rutqvist *et al*., 2007; Ferronato *et al*., 2010; Vilarrasa *et al*., 2010b; Goerke *et al*., 2011; Rutqvist, 2012). The main concern is to guarantee that the mechanical stability of the caprock will not be compromised in order to prevent CO_2 leakage. Nimtz *et al*. (2010) argue that, when injecting liquid CO_2, the overpressure at the bottom of the well will be too high because CO_2 pressure at the wellhead has to be enough to ensure liquid conditions; and the hydrostatic pressure in the well will be also high because liquid CO_2 has a density around 900 kg/m^3. However, they do not perform any hydro-mechanical simulation to confirm their hypothesis. Moreover, they do not consider reducing temperature, which ensures liquid conditions with moderate pressures. Note that an excessive overpressure can induce microseismicity (Phillips *et al*., 2002; Guglielmi *et al*., 2008; Cappa and Rutqvist, 2011), which may open up migration paths for CO_2. However, since liquid CO_2 is colder than the formations where it will be injected, liquid CO_2 injection implies a combination of hydro-mechanical and thermo-mechanical effects that should be studied simultaneously to properly evaluate the caprock mechanical stability.

The injection of a cold fluid induces a thermal contraction of the rock, leading to a reduction of the effective stresses (Segall and Fitzgerald, 1998), which tends to bring the stress state closer to failure conditions. Thermo-mechanical effects have been studied specially in geothermal reservoir stimulation (Ghassemi *et al*., 2007; Majer *et al*., 2007). The thermo-mechanical effects of injecting CO_2 at a colder temperature than that of the reservoir have been investigated at the In Salah injection project (Algeria), where CO_2 is injected in supercritical conditions, but significantly cooler than the formation (Bissell *et al*., 2011; Preisig and Prévost, 2011; Rutqvist, 2012). Additionally,

non-isothermal CO_2 flow simulations have been performed, but without considering the mechanical coupling and always in supercritical conditions (Han *et al*., 2010; Singh *et al*., 2011). Therefore, the thermo-mechanical effects of liquid CO_2 injection remain to be studied.

We propose to inject CO_2 in liquid state as a new engineering methodology for minimizing energy costs and phase changes in the capture-transport-injection chain, and improving the short- and long-term storage efficiency of CO_2. This injection concept will be tested at the pilot site of Hontomín (Carrera *et al*., 2011a), Burgos, Spain, which is the injection site of the CO_2 storage Technology Demonstration Plant (TDP) of the Compostilla OXYCFB300 project (EU funded: European Energy Programme for Recovery), operated by Fundación Ciudad de la Energía (CIUDEN). Hontomín is a dome-like structure with a dolomitized reservoir located at 1450 m depth, which is overlaid by a caprock made of marls. Several experiments are planned both for site characterization and for injection technology development (Carrera *et al*., 2011a).

The objective of this work is to analyze liquid CO_2 injection into a deep aquifer in terms of (1) the energetic efficiency and (2) caprock mechanical stability. This represents a first step towards the design of the liquid CO_2 injection test that will be performed at the Hontomín pilot test. We calculate CO_2 flow in both the injection well and the reservoir. We perform simulations of non-isothermal two-phase flow in a deformable porous media to evaluate mechanical stability of the caprock.

2.- MATHEMATICAL AND NUMERICAL METHODS

We first solve CO_2 injection in a vertical injection well and afterwards in a saline formation. The geometry of the problem consists in a homogeneous 100 m thick horizontal aquifer that is overlaid and underlain by a seal. The system is axisymmetric and extends 20 km laterally. The nature of the outer hydraulic boundary condition does not affect the results because the radius of the pressure perturbation cone is smaller than the radius of the domain for the injection time scales presented here. Therefore, the model behaves as an infinitely acting aquifer. The top of the aquifer is located at a depth of 1500 m, which corresponds to the depth of the reservoir at the Hontomín test site. The seals that overlay (caprock) and underlie the aquifer have a thickness of 200 m. We assume that the caprock is covered by a 1300 m thick overburden of such a low shear stiffness that does not need to be included in the model. An injection well with a radius of 0.15 m is placed in the center of the domain. This radius was initially planned at Hontomín, but has now been reduced.

2.1.- NON-ISOTHERMAL FLOW IN THE INJECTION PIPE

Flow of CO_2, or any fluid, and its mixtures in non-isothermal wells involves solving the partial differential equation (PDE) that express energy, mass and momentum conservation. These PDEs are coupled through the equations of state (EOS) governing fluid and thermodynamic properties. Several authors describe numerical procedures to solve these equations (Lu and Connell, 2008; Paterson *et al*., 2008; Pan *et al*., 2009; Han *et al*., 2010).

Here, we adopted the approach of Lu and Connell (2008). They presented a methodology to solve steady state non-isothermal multiphase flow of CO_2 in an injection well, in which the flow equations are based on the averaged-flow model (e.g. Brill and Mukherjee, 1999; Hasan and Kabir, 2002). We assume that the steady state assumption describes reasonably well the operation after the initial stages. This leads to a system of one dimensional ordinary differential equation (ODE) along the vertical coordinate, z [L]. The number of equations of such system is five for single-phase conditions or twelve for two-phase conditions. The corresponding vectors of unknown state variables are $\mathbf{x} = (\rho, v, p, h, T)^t$ or $\mathbf{x} = (\theta_l, \rho_l, \rho_g, v, p, h, T, X, s_l, s_g, h_l^{sat}, h_g^{sat})^t$, respectively, where ρ [M L^{-3}] is density, v [L T^{-1}] is velocity of the fluid mixture, p [M L^{-1} T^{-2}] is pressure, h [L^2 T^{-2}] is specific enthalpy, T [Θ] is temperature, θ_l [L^3 L^{-3}] is volumetric liquid content, X [M M^{-1}] is gas mass fraction and s [L^2 T^{-2} Θ^{-1}] is entropy. Subscript *l* and *g* stand for liquid and gas phases, respectively; and superscript *sat* and *t* refer to saturation conditions and to transpose, respectively.

Because solubility of gas into water is neglected, this approach is restricted to pure CO_2 or a multi-component gaseous mixture rich in CO_2, but not a fluid mixture of water and gas. As explained by Lu and Connell (2008), the phase equilibrium condition is checked to identify the state of the fluid at a given point when solving the system of equations. If more than one root of the EOS exists and the Gibbs equilibrium condition applies, then the fluid is identified to be in a two-phase coexistence state and the size of the system is 12. Otherwise, the fluid is in single-phase conditions and the size of the system is 5. It should be noted that the above model simplifies considerably when simulating the injection of liquid CO_2, because single-phase conditions (liquid and/or supercritical) prevail along the entire wellbore.

In the approach of Lu and Connell (2008) the fluid in the injection pipe exchanges heat laterally with its surroundings. The heat exchange term is represented by

$$Q = -2\pi R_p U_\infty \left(T - T_{geo}(z)\right), \quad (1)$$

where U_∞ [M T^{-3} Θ^{-1}] is the overall heat transfer coefficient for the injection well comprising the thermal properties of all the materials and fluids composing it (the injection fluid, the injection pipe wall, the annulus between injection pipe and casing, the casing, the cement and the rock), R_p is the radius of the injection pipe and $T_{geo}(z)$ is the geothermal temperature along the wellbore. We assumed a geothermal gradient of 0.033 ºC/m and a surface temperature of 5 ºC in all the simulations. The internal diameter of the injection pipe is set either at 9.0 and 15.24 cm depending on the injection condition. The bottom of the injection pipe is located at 1500 m, coinciding with the top of the aquifer for CO_2 storage.

To solve the system of flow equations, we need to specify 4 boundary conditions related to the primary physical quantities p, T and v. Additionally, the gas mass fraction X or the volumetric liquid content θ_l need to be specified if injecting two-phase CO_2. Common operational conditions of an injection well imply specifying the pressure and/or the flow rate and the temperature at the wellhead, and a free exit (no dispersive) heat flux at the well bottom. If a pressure-controlled injection condition is assumed at the wellhead, the corresponding flow rate and pressure at the bottom of the well can be specified as boundary conditions in the reservoir multiphase flow model. In fact, this boundary condition facilitates coupling between the injection well and the reservoir. We study flow through the injection well and flow in the formation separately to facilitate the analysis of the processes occurring in each of them in a clear way. However, we

couple them by choosing a pressure and temperature conditions at the wellhead, such that the resulting pressure and temperature conditions at the bottom of the well coincide with the boundary conditions of the two-phase flow simulations in the reservoir.

As far as fluid properties are concerned, density was calculated assuming the Redlich-Kwong EOS (Redlich and Kwong, 1949) using the parameters proposed for CO_2 by Spycher *et al*. (2003). Viscosity was calculated according to the correlation of Altunin and Sakhabetdinov (1972). The friction factor of the fluid through the injection pipe was calculated according to the Blasius equation (Brill and Mukherjee, 1999; Hassan and Kabir, 2002). Turbulent flow can be also calculated using other empirical correlations that include rugosity of the pipe (e.g., Colebrook, 1939; Zigrang and Sylvester, 1985).

The steady state non-isothermal multiphase flow governing equations in the injection pipe were programmed in MatLab. These equations were solved using a variable order method for stiff differential equations. The code was verified by comparison with the solutions presented by Lu and Connell (2008).

2.2.- NON-ISOTHERMAL TWO-PHASE FLOW IN A DEFORMABLE POROUS MEDIUM

Consider CO_2 injection in a deep confined deformable saline formation. In general, the injected CO_2 will not be in thermal equilibrium with the reservoir, especially at high flow rates (Paterson *et al*., 2008). To account for these processes, thermo-hydro-mechanical coupling should be acknowledged. Therefore, mass conservation of each phase, energy balance and momentum balance have to be solved simultaneously.

2.2.1.- Fluid mass conservation equation

Mass conservation of each phase can be expressed as (Bear 1972),

$$\frac{\partial(\varphi S_\alpha \rho_\alpha)}{\partial t} + \nabla \cdot (\rho_\alpha \mathbf{q}_\alpha) = r_\alpha, \qquad \alpha = c, w, \tag{2}$$

where φ [L^3 L^{-3}] is porosity, S_α [-] is saturation of the α -phase, ρ_α [M L^{-3}] is density, t [T] is time, $\mathbf{q}_\alpha$ [L^3 L^{-2} T^{-1}] is the volumetric flux, r_α [M L^{-3} T^{-1}] is the phase change term (i.e. CO_2 dissolution into water and water evaporation into CO_2) and α is either CO_2 rich phase, c, or aqueous phase, w. For the sake of simplicity we neglect evaporation of water into CO_2, i.e., $r_w = 0$.

Momentum conservation is expressed using Darcy's law, written as

$$\mathbf{q}_\alpha = -\frac{k k_{r\alpha}}{\mu_\alpha}(\nabla p_\alpha + \rho_\alpha g \nabla z), \qquad \alpha = c, w, \tag{3}$$

where k [L^2] is intrinsic permeability, $k_{r\alpha}$ [-] is the α -phase relative permeability, μ_α [M L^{-1} T^{-1}] its viscosity, p_α [M L^{-1} T^{-2}] its pressure and g [L T^{-2}] is gravity.

The properties of the aquifer and seals correspond to those of limestone and shale, respectively. Their values have been taken mainly from Vilarrasa *et al*. (2010b) and updated from the current knowledge on the rock properties of the Hontomín test site, and are detailed in Table 1. We consider the aquifer to be a permeable limestone with homogeneous grain size. Therefore, the entry pressure is low and the shape parameter of the van Genuchten (1980) retention curve is high. On the other hand, seal entry pressure is high, which hinders CO_2 migration. Relative permeabilities follow a power law of saturation for both phases: the limestone has a cubic law, while the power in the seals is

6. The difference in the exponents reflects that low-permeability rocks usually present higher multiphase interference effects than high-permeability rocks (Bennion and Bachu, 2008). CO_2 density and viscosity are highly dependent on p and T conditions (Garcia, 2003).

Buoyancy effects are relevant in the CO_2 plume evolution, regardless of injection conditions. However, when injecting liquid CO_2 the density contrast between CO_2 and brine is smaller than when injecting SC CO_2. Additionally, liquid CO_2 viscosity is higher than SC CO_2 viscosity. Thus, viscous forces gain strength in front of gravity forces under liquid condition. This can be quantified through the gravity number, which compares viscous forces (evaluated for radial flow at the characteristic length) with buoyancy (Vilarrasa *et al*., 2010a)

$$N_g = \frac{2\pi r_c b k k_{r\alpha} \Delta\rho g \rho_c}{Q_m \mu_c}, \tag{4}$$

where r_c [L] is a characteristic length, b [L] is aquifer thickness, $\Delta\rho$ [M L^{-3}] is the difference between CO_2 and water density and Q_m [M T^{-1}] is the CO_2 mass flow rate. The characteristic length depends on the scale of interest (Kopp *et al*., 2009; Vilarrasa *et al*., 2010a).

2.2.2.- Energy conservation equation

Energy conservation can be written as (e.g., Faust and Mercer, 1979)

$$\frac{\partial\left((1-\varphi)\rho_s h_s + \varphi\rho_w S_w h_w + \varphi\rho_c S_c h_c\right)}{\partial t} - \frac{\partial\left(\varphi S_w p_w + \varphi S_c p_c\right)}{\partial t} + \nabla\cdot\left(-\lambda\nabla T + \rho_w h_w \mathbf{q}_w + \rho_c h_c \mathbf{q}_c\right) = 0, \tag{5}$$

where ρ_s [M L^{-3}] is solid density, h_α [L^2 T^{-2}] is enthalpy of α-phase ($\alpha = c, w, s$; s for solid) and λ [M L T^{-3} Θ] is thermal conductivity.

Eq. (5) includes non-isothermal processes, such as Joule-Thomson effect (Tsang *et al*., 2008), heat of CO_2 dissolution and water evaporation (Han *et al*., 2010) and compression work due to the high compressibility of CO_2. We consider all these processes, except water evaporation.

2.2.3.- Thermoelasticity in porous media

To solve the mechanical problem, the momentum balance of the porous media has to be satisfied. If inertial terms are neglected, it reduces to the equilibrium of stresses

$$\nabla \cdot \boldsymbol{\sigma} + \mathbf{b} = \mathbf{0}\,, \tag{6}$$

where $\boldsymbol{\sigma}$ [M L^{-1} T^{-2}] is the stress tensor and $\mathbf{b}$ [M L^{-2} T^{-2}] is the body forces vector.

Furthermore, we assume that the medium behaves elastically. In fact, we use linear thermoelasticity to acknowledge the effect of changes in fluid pressure and temperature. Therefore, assuming that the compressibility of the solid phase is negligible compared to that of the drained bulk material (so Biot's coefficient, which multiplies pressure in the effective stress equation, equals 1), elastic strain depends on total stress, overpressure and temperature as (Biot, 1956)

$$\boldsymbol{\varepsilon} = \frac{1+\nu}{E}\boldsymbol{\sigma} - \frac{3\nu}{E}\sigma_m \mathbf{I} - \frac{1-2\nu}{E}\Delta p \mathbf{I} - \alpha_T \Delta T \mathbf{I}\,, \tag{7}$$

where $\boldsymbol{\varepsilon}$ [L L^{-1}] is the strain tensor, $\sigma_m = \left(\sigma_x + \sigma_y + \sigma_z\right)/3$ [M L^{-1} T^{-2}] is the mean stress, $\mathbf{I}$ [-] is the identity matrix, E [M L^{-1} T^{-2}] is the Young's modulus, ν [-] is Poisson ratio and α_T [Θ^{-1}] is the thermal expansion coefficient. Here, the sign criterion

of geomechanics is adopted, i.e. strain is positive in compression and negative in extension.

The simulations that will be shown in section 4 suggest that the temperature perturbation is localized within a relatively small volume of the formation close to the injection well, thus acting spherically. However, the fluid pressure perturbation propagates a long distance in the direction of the aquifer, but not in the perpendicular, thus acting anisotropically. Therefore, an approximate estimate of stress changes can be obtained by assuming that stresses vary isotropically with temperature changes and that no horizontal strain is allowed in the outer boundary as a result of lateral confinement. This leads to a variation of the vertical and horizontal stresses as a result of fluid pressure and temperature variations as

$$\Delta\sigma_v = \frac{E}{(1-2\nu)}\alpha_T \Delta T \,, \tag{8a}$$

$$\Delta\sigma_h = \frac{1-2\nu}{1-\nu}\Delta p + \frac{E}{(1-2\nu)}\alpha_T \Delta T \,, \tag{8b}$$

where σ_v [M L^{-1} T^{-2}] is the vertical stress and σ_h [M L^{-1} T^{-2}] is the horizontal stress.

Eq. (8b) shows that an increase in pore pressure and/or temperature, which produces an expansion of the porous media, causes an increase of horizontal stresses because of lateral confinement that opposes to the induced expansion. On the other hand, a decrease in temperature, which produces a contraction of the porous media, causes a decrease of horizontal stresses. Notice that pressure variations do not affect much the total vertical stress, which remains largely lithostatic for our problem set up, as discussed below.

2.2.4.- Model setup

The initial conditions are hydrostatic pressure; temperature following a geothermal gradient of 0.033 ºC/m, with a surface temperature of 5 ºC; a vertical stress gradient of 0.023 MPa/m. The value of the lateral earth pressure coefficient at the Hontomín test site cannot be determined from the existing data. The geological indicators suggest a normal faulting stress regime, i.e. a lateral earth pressure coefficient lower than 1.0, but its actual value will not be possible to determine until drilling of the wells. To address this uncertainty, we adopt horizontal effective stresses corresponding to a lateral earth pressure coefficient of either 0.5 (vertical stress larger than horizontal stresses) or 2.0 (horizontal stresses larger than vertical stress). As a first step, a steady-state calculation is carried out to ensure consistent initial conditions in equilibrium for the pressure, temperature and stress fields.

The hydraulic boundary conditions are a prescribed CO_2 mass flow rate at the injection well (1.0 Mt/yr), a constant pressure on the outer boundary and no flow at the top and bottom boundaries. The thermal boundary conditions are constant temperature at the top and bottom boundaries of the domain. Neither pressure nor thermal perturbations reach the top and bottom boundaries, so the nature of these boundary conditions does not affect the results. The mechanical boundary conditions are no displacement normal to the bottom, outer and injection well boundaries. A constant, vertical lithostatic stress is imposed at the top of the caprock.

The mesh is made of structured quadrilateral elements. Laterally, the size of the elements is of tens of cm close to the injection well and increases exponentially up to a longitudinal size of 400 m next to the outer boundary. Vertically, the elements within

the aquifer are of 5 m. In the caprock, they grow from 5 m at the contact with the aquifer to 25 m far away from it.

Non-isothermal CO_2 injection in a deformable porous media is simulated using the finite element numerical code CODE_BRIGHT (Olivella *et al*., 1994, 1996). We have implemented CO_2 properties, such as density, viscosity, enthalpy and heat capacity, discussed in sections 2.2.1 and 2.2.2, in order to simulate CO_2 storage. Furthermore, we have incorporated in the energy conservation the term of CO_2 volumetric compression due to pressure changes (second term of Eq. (5)), maintaining temperature as the state variable.

2.3.- MECHANICAL STABILITY

To determine whether a pre-existing fracture is stable or not, a failure criterion needs to be defined. The medium is stable and behaves elastically while the stress state falls inside the failure envelope. However, if the stress state touches the failure envelope, the rock yields, producing a microseismic event. We adopt the Mohr-Coulomb failure criterion

$$\tau = c' + \sigma'_n \tan \phi' , \qquad (9)$$

where τ [M L^{-1} T^{-2}] is the shear stress, σ'_n [M L^{-1} T^{-2}] is the normal effective stress, c' [M L^{-1} T^{-2}] is cohesion and ϕ' [-] is the friction angle.

The effective stress tensor, considering the sign criterion of geomechanics, i.e. stress and fluid pressure are positive in compression, is defined as

$$\boldsymbol{\sigma}' = \boldsymbol{\sigma} - p\mathbf{I}, \tag{10}$$

where $\boldsymbol{\sigma}'$ [M L^{-1} T^{-2}] is the effective stress tensor and $p = \max(p_w, p_c)$ [M L^{-1} T^{-2}] is fluid pressure.

We assume an axisymmetric initial stress state in which the horizontal effective stress is

$$\sigma'_h = k_0 \sigma'_v, \tag{11}$$

where k_0 [-] is the lateral earth pressure coefficient. The stress regime has a great effect on the caprock failure mechanisms (Rutqvist *et al*., 2008; Vilarrasa *et al*., 2011b). Therefore, the effect of k_0 should be investigated.

Let us assume that a fracture exists with a dip angle θ [-] (Figure 2). If we assume that the fracture is cohesionless, the mobilized friction angle can be calculated from Eq. (9) considering the stress changes induced by overpressure and temperature changes (Eq. (8)) in the normal effective stress and the shear stress that act on this pre-existing fracture, which yields

$$\tan \phi'_{mob} = \frac{0.5\left[\sigma'_{v0}(1-k_0) - (1-2\nu)/(1-\nu)\Delta p\right]\sin 2\theta}{\sigma'_{v0}\left[1-(1-k_0)\sin^2\theta\right] + \left[(1-2\nu)/(1-\nu)\sin^2\theta - 1\right]\Delta p + E/(1-2\nu)\alpha_T \Delta T} \tag{12}$$

where σ'_{v0} [M L^{-1} T^{-2}] is the original vertical effective stress, i.e. prior to pore pressure and temperature changes. The mobilized friction angle is a measure of how close to failure is the fracture. The closer the mobilized friction angle is to the actual friction angle, the closer to failure is the fracture.

It can be demonstrated geometrically by using the Mohr circle to represent the stress state that the dip angle of the most critically oriented fracture, θ_{cr}, is related to the friction angle of the fracture by

$$\theta_{cr} = \frac{\pi}{4} + \frac{\phi'}{2}, \quad \text{if } k_0 < 1, \tag{13a}$$

$$\theta_{cr} = \frac{\pi}{4} - \frac{\phi'}{2}, \quad \text{if } k_0 > 1. \tag{13b}$$

Assuming that a cohesionless fracture exists in the critical dip angle, the overpressure that will produce failure of this pre-existing fracture for a given friction angle, depth, lateral earth pressure coefficient and temperature change is

$$\begin{aligned}
&\frac{\Delta p}{\sigma'_{v0}} = \frac{2(1-\nu)}{1-2\nu-\sin\phi'}\left[1-0.5(1+k_0)(1+\sin\phi') - \frac{E}{(1-2\nu)\sigma'_{v0}}\alpha_T \Delta T \sin\phi'\right], \\
&\text{if } k_0 < 1 - \frac{1-2\nu}{1-\nu}\frac{\Delta p}{\sigma'_{v0}} \\
&\frac{\Delta p}{\sigma'_{v0}} = \frac{2(1-\nu)}{1-2\nu+\sin\phi'}\left[1-0.5(1+k_0)(1-\sin\phi') + \frac{E}{(1-2\nu)\sigma'_{v0}}\alpha_T \Delta T \sin\phi'\right], \\
&\text{if } k_0 > 1 - \frac{1-2\nu}{1-\nu}\frac{\Delta p}{\sigma'_{v0}}
\end{aligned} \tag{14}$$

Alternatively, the temperature change that will produce failure of this pre-existing cohesionless fracture for a given friction angle, depth, lateral earth pressure coefficient and overpressure is

$$\Delta T = \frac{(1-2\nu)\sigma'_{v0}}{E\alpha_T \sin\phi'}\left[1-0.5(1+k_0)(1+\sin\phi')-\frac{1-2\nu-\sin\phi'}{2(1-\nu)}\frac{\Delta p}{\sigma'_{v0}}\right],$$
$$\text{if } k_0 < 1-\frac{1-2\nu}{1-\nu}\frac{\Delta p}{\sigma'_{v0}}$$
$$\Delta T = \frac{(1-2\nu)\sigma'_{v0}}{E\alpha_T \sin\phi'}\left[-1+0.5(1+k_0)(1-\sin\phi')+\frac{1-2\nu+\sin\phi'}{2(1-\nu)}\frac{\Delta p}{\sigma'_{v0}}\right], \quad (15)$$
$$\text{if } k_0 > 1-\frac{1-2\nu}{1-\nu}\frac{\Delta p}{\sigma'_{v0}}$$

3.- NON-ISOTHERMAL CO_2 FLOW IN THE INJECTION WELL

We consider several operational conditions at the wellhead to compare the feasibility and energy consumption of the proposed injection concept with other schemes. We use the methodology of Section 2 to simulate non-isothermal multiphase flow of CO_2 through the injection well in gas, supercritical and liquid phase.

3.1.- CO_2 BEHAVIOR IN THE INJECTION WELL

Table 2 displays the pressure and temperature values for five injection conditions at the wellhead: gas-phase, near-critical point, supercritical phase, liquid-phase at high pressure and temperature and liquid-phase at low pressure and temperature. A mass flow rate of 1.5 kg/s, which corresponds to an injection rate typical of a pilot site (injection rates ranging from 0.05 to 2.0 kg/s will be tested at Hontomín), and an overall heat transfer coefficient of $U_\infty = 10$ W m^{-2} K^{-1}, were considered in the simulations. The assumed value of U_∞ is representative of a typical injection well formed by the cement, a steel casing, an annular space filled with brine, a steel injection pipe and the CO_2 within the pipe (e.g., Lu and Connell, 2008; Brill and Mukherjee 1999). In practice, this value will drop with time as the rock surrounding the well cools downs, which has been

neglected here, but will be addressed in the sensitivity analysis. Figure 3 displays the temperature, pressure and density profiles obtained for each injection conditions.

Figure 3 shows that injection in gas and supercritical phase conditions causes a distribution of low densities along the wellbore. Injecting gaseous CO_2 in near-critical point conditions causes a two-phase flow pattern within the injection pipe near the surface (in the first 50 m). It should be noted that phase changes always lead to higher head losses in pipes. This two-phase flow behavior is associated with a change in the slope of the temperature profile when the fluid becomes supercritical. The resulting change of phase leads to higher densities through the injection pipe than those obtained when injecting in gas and supercritical phase conditions.

In contrast, the injection of CO_2 in liquid-phase conditions leads to a high CO_2 density, which is comparable to that of brine, along the entire injection pipe. CO_2 temperature stays nearly constant through a long section of the pipe and then increases slightly due to heat exchange with the surroundings. Actually, when injecting at high pressure and temperature, the fluid undergoes a small cooling in the upper portion because of the heat exchange with the geological media. On the other hand, CO_2 pressure at the bottom of the well becomes very high, around 20 MPa for this particular injection conditions, because the injection at the wellhead is made at high pressure. However, a smaller overpressure can be obtained at the bottom of the well by injecting liquid CO_2 at low pressure and temperature, resulting in a CO_2 pressure similar to that obtained when injecting in near-critical conditions, i.e. around 17 MPa.

The overall heat transfer coefficient is a parameter that depends on the different thermal properties of the materials and fluids involved in the injection well (cement, casing, tubing, etc.). U_∞ is also time dependent and for high temperature it depends on

temperature as well. U_∞ can be calculated according to the methods described in Willhite (1967), Brill and Mukherjee (1999), and Hasan and Kabir (2002). As the overall heat transfer coefficient can take a wide range of values, we analyze the sensitivity of results to this parameter. Injection temperature and pressure were set at 5 ºC and 4.2 MPa, respectively. Figure 4 displays the results obtained when varying U_∞ between 0.1 and 1000 W m^{-2} K^{-1}. Conditions reached by the fluid at the bottom of the well are supercritical for high values of the overall heat transfer coefficient (U_∞ = 100, 1000 W m^{-2} K^{-1}), which induce a thermal equilibrium between the fluid and the geological media. It is evident that the fluid within the injection pipe receives less heat from its surroundings by enhancing the thermal insulation of the wellbore, i.e. reducing U_∞. This helps keeping low temperatures through the injection pipe (Figure 4a), leading to CO_2 density values that approach those of water density (Figure 4c).

Sensitivity to injection temperature is displayed in Figure 5, which depicts the temperature, pressure and density distributions along the injection well for five injection temperatures and a wellhead pressure of 4.2 MPa. The overall heat transfer coefficient and the CO_2 mass flow rate were set at 10.0 W m^{-2} K^{-1} and 1.5 kg/s, respectively. A reduction in the injection temperature of 25 ºC (with respect to 5 ºC) causes a density increase of only 7% at the bottom of the injection pipe, while the pressure increase is lower than 2.0 MPa.

To compare SC CO_2 injection with injection of liquid CO_2 at industrial scale we also run two additional simulations for a CO_2 injection mass flow rate of 1.0 Mt/yr. Operational conditions and parameters for each case are shown in Table 3. We consider here the overall heat transfer coefficient as a design parameter (e.g., it can be modified by choosing appropriate materials: steel for high values of U_∞; or fiber glass or

insulating fluid, such as silicone, for low values of U_∞) such that the differences in the overall heat transfer coefficient can be representative of different dimensions of the wellbore (e.g. diameter of injection pipe), different construction materials, different type of cements, use of isolating mechanisms, and variations induced by the dynamic of the operation before achieving steady state conditions. In these simulations we have assumed a value of U_∞ that ensure liquid conditions along the whole injection pipe in one case, and allows to control the bottom pressure in the case of SC CO_2 injection. The pressure, temperature and density profiles obtained for each injection strategy are shown in Figure 6. When injecting SC CO_2 the temperature at the bottom of the well is around 56 ºC, which corresponds to the mean temperature of the aquifer placed at 1500 m depth considered in our simulations. In contrast, injecting CO_2 in liquid conditions along the entire injection pipe yields a temperature at the bottom of the well around 20 ºC. Pressure at the bottom of the well is approximately 17 MPa in both cases, whereas the wellhead pressure in the liquid case is about one third of that in the supercritical case. These downhole fluid conditions are consistent with the boundary conditions in the simulation of CO_2 injection presented in Section 4.

3.2.- ENERGY CONSUMPTION ANALYSIS

At pilot sites, CO_2 is often stored in vessels at very low temperatures (≈ -20 ºC) and pressures in the order of 2.0 MPa. The energy consumption associated to surface conditioning operations, such as compression, pumping and heating, will vary for each injection mode. Normally, to obtain the desired pressure and temperature conditions for injection, CO_2 is first pumped/compressed and then heated. To analyze the energy consumption of these operations we can use macroscopic energy balances. For

negligible heat transfer with the surroundings and no appreciable kinetic and potential energy effects, the energy rate balance reduces, at steady state, to the work input per unit of mass flowing through a compressor or a pump as the specific enthalpy difference between the exit and the inlet of the compressor/pump (Moran *et al.*, 2011). A similar estimation can be made to calculate the energy demand during heating. Therefore, the total energy consumed to reach the injection conditions can be roughly estimated by the difference of specific enthalpy between wellhead and storage vessel conditions.

Table 2 includes the energy consumption of the five injection modes, calculated assuming that the pressure and temperature of the storage vessel are 2.0 MPa and -20 ºC, respectively. Table 2 shows that the energy consumption is higher when injecting CO_2 in gas-phase, near-critical and supercritical conditions at the wellhead. On the other hand, and as expected, injecting CO_2 in liquid-phase at the wellhead reduces the energy consumption because pumping/compression is easier and heating is minor. The injection of liquid CO_2 at low temperature and pressure involves the lowest energy consumption. For a given injection pressure (Figure 5), energy consumption due to heating at the surface decreases as the wellhead temperature decreases (considering a storage temperature of -20 ºC). Figure 7 shows that, at pilot scale, injecting at low temperatures may involve an energy saving in the order of 300 %. Notice also, that depending on local conditions, transport pressure may be higher than required for injection, which would allow recovering some energy. Energy recovery would be largest for cold, low pressure, liquid injection.

The energy consumption for a CO_2 mass flow rate of 1.0 Mt/yr, assuming the surface storage pressure and temperature conditions of the pilot test site of Hontomín (2.0 MPa and -20 ºC), is 7910 kW for SC CO_2 injection, while it is just of 675 kW for liquid CO_2

injection. However, a fairer comparison for such a high mass flow rate should consider pressure and temperature values resulting from transport through a long CO_2 pipeline. CO_2 transport and injection scenarios simulated by Nimtz *et al.* (2010) showed that CO_2 can arrive at the injection site at 8.5 MPa and 12 ºC. Thus, to get the injection conditions shown in Table 3, SC CO_2 injection would require a combination of heating and throttling, while cold CO_2 injection would require cooling and expansion (see Figure 8). Furthermore, energy could be produced in the CO_2 expansion by passing the expanding CO_2 through a turbine. Based on these hypothetical conditioning operations, the resulting energy cost is 5820 kW and -1415 kW for SC and liquid CO_2 injection, respectively (the negative sign indicates that energy can be produced). Interestingly, if CO_2 is injected at the wellhead conditions proposed by Nimtz *et al.* (2010) in their application, i.e. 8.5 MPa and 12 ºC at the end of the pipeline and a mass flow rate of 117.3 kg/s distributed in 60 injection wells (1.95 kg/s in each well), CO_2 would reach the aquifer at 17.5 MPa and 35 ºC. Since the bottom hole pressure is similar to that of the reservoir simulation (see Section 4), CO_2 could be injected directly from the pipeline without any conditioning operation. Therefore, both at pilot and industrial scales injecting CO_2 in liquid phase conditions leads to a much lower energy demand.

The results of the simulations presented in this section show that it is possible to inject CO_2 in dense liquid-phase by controlling the operational variables, which could lead to a significant reduction of the operational energy costs.

4.- THERMO-HYDRO-MECHANICAL EFFECTS OF LIQUID CO_2 INJECTION

4.1.- THERMAL EFFECTS ON CO_2 PLUME EVOLUTION

Liquid CO_2 is denser and more viscous than SC CO_2. This means that gravity forces lose strength in front of viscous forces, which leads to a steeper CO_2-brine interface close to the injection well (Figure 9), where CO_2 remains in liquid state (Figure 10a). Further away, where CO_2 reaches SC conditions, the CO_2 plume evolution is characterized by gravity override (Nordbotten *et al*. 2005; Dentz and Tartakovsky, 2009; Vilarrasa *et al*., 2010a) (Figure 9). The thermal transition is abrupt (Figure 10b). Once cold liquid CO_2 enters in the aquifer, it heats up until thermal equilibrium is reached, so that CO_2 evolves to SC conditions as it flows away from the well. Therefore, the liquid CO_2 region is much smaller than the whole CO_2 region. This leads to a steep liquid CO_2 front (where viscous forces dominate gravity forces) that advances behind the typical CO_2 plume interface (where gravity forces dominate viscous forces).

Apart from the cold CO_2 injection, several processes affect the temperature distribution of the CO_2 plume. There is an interaction between: (1) the warmer CO_2 placed at the bottom of the aquifer, which flows upwards along the interface, (2) the colder brine placed at the top of the aquifer, which flows downwards along the interface, (3) CO_2, which cools down as it advances away from the injection well due to the Joule-Thomson effect and (4) temperature increases due to the exothermal reaction of CO_2 dissolution into the brine. The net result of these processes is a slight temperature increase in the SC CO_2 region (Figure 10b).

Figure 11a shows that injection pressure for liquid CO_2 is slightly smaller than that of SC CO_2 because a higher CO_2 density reduces the volumetric flow rate and therefore the pressure buildup around the well. This is energetically advantageous, because a smaller compression work has to be done to inject the same amount of CO_2. Furthermore, the overpressure in the whole aquifer becomes smaller (Figure 11b), which improves the mechanical stability of the caprock.

4.2.- MECHANICAL RESPONSE TO LIQUID CO_2 INJECTION

These pressure and temperature changes induce strain and stress changes. Figure 12 displays the horizontal and vertical displacements of SC and liquid CO_2 injection. Since fluid pressure distribution is quite similar in both injections (recall Figure 11), the differences in displacements will be due to thermal effects. SC CO_2 injection (isothermal) produces a vertical expansion of the aquifer, pushing upwards the caprock and slightly downwards the seal placed below the aquifer. Laterally, SC CO_2 injection pushes the aquifer away from the injection well. However, liquid CO_2 injection generates a cold region around the injection well that undergoes thermal contraction. This is reflected in both the vertical and horizontal displacement. Vertically, the caprock moves downwards and the seal below the aquifer moves upwards close to the injection well. Similarly, the aquifer is displaced towards the injection well in the cold region, presenting the maximum negative horizontal displacement at the cold temperature front. Nevertheless, the thermal effect occurs close to the injection well, where cold CO_2 stays in liquid state (recall Figure 10b). Further away, the aquifer expands, both vertically and horizontally, due to overpressure.

Figure 13 displays total stress changes as a function of depth 3 m away from the injection well after 8 months of injecting liquid and SC CO_2. The stress change is almost symmetric with respect to the middle of the aquifer. The vertical stress remains practically unaltered when injecting SC CO_2. However, it is reduced as a result of temperature drop when injecting liquid CO_2, with the maximum stress reduction in the middle of the aquifer. The stress reduction is also significant in the region of the seals affected by the temperature reduction (recall Figure 10b). The horizontal stresses increase in the aquifer because of lateral confinement that opposes to the expansion caused by CO_2 injection. The stress reduction due to thermal contraction of the rock superimposes to this horizontal stress increment, resulting in a stress reduction in the aquifer when injecting liquid CO_2. The stress reduction due to thermal contraction of the rock is similar in magnitude in the vertical and horizontal directions. The fact that vertical stresses decrease in the aquifer produces an increase of the horizontal stresses in the seals close to their contact with the aquifer. This can be explained by an arch effect that is formed around the volume with vertical stress reduction to be able to support the overburden on top of the aquifer.

The volume where CO_2 stays in liquid state has equilibrated with the rock and formation water, thus displaying a homogeneous temperature and the transition to the geothermal temperature of the aquifer is abrupt (Figure 10b). Therefore, the rock affected by the effective stress reduction due to thermal contraction of the rock presents a homogeneous stress reduction (Figure 13) that is proportional to the temperature drop, the linear thermal expansion coefficient and the bulk modulus of the rock (Eq. (8)). Thus, the thermal effect will dominate for large temperature contrasts and in stiff rocks.

4.3.- MECHANICAL STABILITY RELATED TO LIQUID CO_2 INJECTION

Fluid injection induces an effective stress reduction that brings the stress state closer to the failure envelope. Furthermore, if the fluid is colder than the formation, a thermal contraction of the rock will occur, further reducing the effective stresses. However, liquid CO_2 injection benefits from a lower overpressure for a given mass flow rate (Figure 11). Therefore, coupled thermo-hydro-mechanical effects of liquid CO_2 injection are non-trivial and should be evaluated simultaneously to properly assess the mechanical stability of the aquifer and the caprock.

Figure 14 compares the mobilized friction angle along the vertical at a radial distance of 3 m away from the injection well when injecting liquid and SC CO_2 for two values of the lateral earth pressure coefficient. The mobilized friction angle in the aquifer is higher for liquid CO_2 injection than for SC CO_2 injection. However, the opposite occurs at the seals close to their contact with the aquifer when injecting liquid CO_2 for a lateral earth pressure coefficient of 0.5 (Figure 14a). This is because when the lateral earth pressure coefficient is lower than 1.0, the maximum principal stress is the vertical. Therefore, if the vertical stress is reduced and the horizontal stress increases (recall Figure 13), the Mohr circle becomes smaller, leading to a more stable situation with a smaller mobilized friction angle. The opposite occurs in the aquifer, where the vertical and horizontal stresses are reduced and therefore the Mohr circle shifts to the left, mobilizing higher friction angles. On the other hand, a lateral earth pressure coefficient higher than 1.0 implies a vertical stress smaller than the horizontal stresses. In this situation, a decrease in the vertical stress higher than in the horizontal stress makes the Mohr circle bigger, mobilizing higher friction angles (Figure 14b). This trend is only altered in the aquifer close to the contact with the seals, where the reduction in

horizontal stress is higher than in vertical stress, leading to a local minimum of the mobilized friction angle in the aquifer.

If the mobilized friction angle becomes higher than the actual friction angle, shear slip of critically oriented pre-existing fractures will occur, which would trigger microseismic events. The effect of shear slip can be advantageous while it takes place within the aquifer, because it will enhance permeability, especially in the direction perpendicular to shear due to dilatancy (Yeo *et al*., 1998; Mallikamas and Rajaram, 2005; Vilarrasa *et al*., 2011a), thus increasing injectivity. However, if it extends to the caprock, the open-up of fractures can lead to CO_2 leakage. Liquid CO_2 injection increases significantly the mobilized friction angle in the aquifer (Figure 14), but it improves caprock stability. This could be even advantageous for the energetic efficiency of this injection concept, because an increase in injectivity due to shearing of pre-existing fractures would lead to a lower injection pressure. Nevertheless, caprock stability should be carefully investigated for large temperature contrasts and in stiff rocks because fracture instability could propagate from the aquifer to the lower part of the caprock.

Since thermo-hydro-mechanical simulations have an extremely high computational cost, it is unfeasible to carry out a large number of them. Therefore, we use the analytical expressions of Eqs. (14) and (15) to gain insight into the injection conditions that can yield fracture instability in the aquifer in its contact with the caprock. Figure 15a displays the overpressure normalized by the effective lithostatic stress that is needed to induce a microseismic event at the top of an aquifer placed at 1500 m depth when injecting cold CO_2 as a function of the friction angle for several temperature changes for a lateral earth pressure coefficient of 0.5 and a Poisson ratio of 0.3 using Eq. (14). Obviously, the aquifer can support higher overpressures as its friction angle increases.

But microseismicity is induced within the reservoir by lower overpressures when the temperature contrast increases because the stresses are reduced (Eq. 8). Furthermore, the stiffer the rock, the lower the overpressure needed to reach the failure envelope within the aquifer for a given temperature change.

Figure 15b displays the temperature change that is needed to induce a microseismic event at the top of an aquifer placed at 1500 m depth when injecting cold CO_2 as a function of the friction angle for several overpressures for a lateral earth pressure coefficient of 0.5 and a Poisson ratio of 0.3 using Eq. (15). The maximum acceptable temperature change for a given overpressure increases with the friction angle. Furthermore, the stiffer the rock, the smaller the temperature change required for inducing microseismicity within the reservoir for a given overpressure. Figure 15 can be used as a reference to assess the feasibility of injecting liquid CO_2 at a given site, once the stiffness of the rock and the temperature change are known. Since there are 3D effects that have not been considered in the analytical treatment of the problem, Figure 15 should be used only for guidance. However, its use is strongly recommended as a preliminary analysis of the suitability of liquid CO_2 injection at a given site because they avoid performing coupled thermo-hydro-mechanical simulations, which imply a high computational cost.

6.- CONCLUSIONS

We propose injecting CO_2 in liquid state rather than supercritical. This is favourable for several reasons: (1) this injection strategy is energetically advantageous, (2) no transformation operation or low energy consumption conditioning operations are

necessary, (3) a smaller compression work at the wellhead is necessary because of the smaller compressibility of liquid CO_2, (4) since liquid CO_2 is denser than SC CO_2, liquid CO_2 injection not only requires a much lower pressure at the wellhead, but also induces a slightly lower overpressure within the aquifer because a smaller amount of fluid is displaced and (5) the caprock mechanical stability is improved.

Although relatively simple as a concept, the implementation of the operation may require a thorough design of conditioning systems (e.g. throttling, heating or cooling) to get the injection conditions. Nevertheless, the system is relatively easy to control because direct control variables are the injection temperature and pressure. Additionally, the system may be indirectly controlled by a suitable design of the wellbore materials (e.g. cement, casing) to reduce the heat transfer between the pipe and the surroundings, thus ensuring that the CO_2 remains in liquid state along the entire injection pipe. Since the temperature at which CO_2 will reach the aquifer will be lower than that of the aquifer, non-isothermal simulations should be performed to reproduce realistic injection conditions.

As for the mechanical stability of the rocks, the thermal effect can be pronounced for large temperature contrasts and stiff rocks. Thermal contraction mobilizes higher friction angles in the aquifer, which could lead to shear slip of pre-existing fractures. The effect of shear slip can be advantageous while it takes place within the aquifer, because it enhances permeability and thus CO_2 injectivity. Interestingly, the mobilized friction angle in the seals is not increased when injecting liquid CO_2 and it is even reduced in stress regimes where the maximum principal stress is the vertical.

ACKNOWLEDGEMENTS

V.V. wishes to acknowledge the Spanish Ministry of Science and Innovation (MCI), through the "Formación de Profesorado Universitario" Program, and the "Colegio de Ingenieros de Caminos, Canales y Puertos – Catalunya" for their financial support. This work has been funded by Fundación Ciudad de la Energía (Spanish Government) (www.ciuden.es) through the project ALM/09/018 and by the European Union through the "European Energy Programme for Recovery" and the Compostilla OXYCFB300 project. We also want to acknowledge the financial support received from the 'MUSTANG' (www.co2mustang.eu) and 'PANACEA' (www.panacea-co2.org) projects (from the European Community's Seventh Framework Programme FP7/2007-2013 under grant agreements nº 227286 and nº 282900, respectively).

REFERENCES

Altunin VV, Sakhabetdinov MA (1972).Viscosity of liquid and gaseous carbon dioxide at temperatures 220-1300 K and pressure up to 1200 bar. *Teploenergetika*, **8**: 85–89.

Angus A, Armstrong B, Reuck KM (eds.) (1976): *International thermodynamics tables of the fluid state. Carbon dioxide*. International Union of Pure and Applied Chemistry. Pergamon Press, Oxford.

Bachu S (2003). Screening and ranking of sedimentary basins for sequestration of CO_2 in geological media in response to climate change. *Environ. Geol*. **44**: 277–289.

Bear J (ed.) (1972). *Dynamics of fluids in porous media*. Elsevier, New York.

Bennion B, Bachu S (2008). Drainage and imbibition relative permeability relationships for supercritical CO_2/brine and H_2S/brine systems in intergranular sandstone, carbonate, shale, and anhydrite rocks. *SPE Reservoir Evaluation & Engineering*, **11**:487-496.

Biot MA (1956). Thermoelasticity and irreversible thermodynamics. *Journal of Applied Phisics* **27(3)**:240-253.

Bissell RC, Vasco DW, Atbi M, Hamdani M, Okwelegbe M,Goldwater MH (2011). A full field simulation of the In Salah gas production and CO_2 storage project using a coupled geo-mechanical and thermal fluid Flow simulator. *Energy Procedia*, **4**:3290-3297.

Bolster D, Dentz M, Carrera J (2009). Effective two-phase flow in heterogeneous media under temporal pressure fluctuations. *Water Resources Research*, **45**, W05408, doi: 1029/2008WR007460.

Brill J, Mukherjee H (1999). Multiphase flow in wells. Henry L. Doherty Memorial fund of AIME, Society of Petroleum Engineers Inc., Richardson, Texas.

Burton M, Bryant SL (2009). Surface dissolution: minimizing groundwater impact and leakage risk simultaneously. *Energy Procedia*, **1**: 3707-3714.

Cappa F, Rutqvist J (2011). Impact of CO_2 geological sequestration on the nucleation of earthquakes. *Geophysical Research Letters*, **38**, L17313, doi: 10.1029/2011GL048487.

Carrera J, Silva O, Rötting T, Carbonell R, Vilarrasa V, Pérez-Estaún A, CIUDEN's research group (2011a). Characterization and working programme of Hontomín

CO_2 injection site (Spain). Monitoring, hydrogeochemical characterization and injection tests. *6th Trondheim Carbon, Capture and Sequestration Conference,* 14-16 June, Trondheim, Norway.

Carrera J, Silva O, Ayora C (2011b). Método y sistema de almacenamiento de gases solubles en formaciones geológicas permeables. *European patent application Nº EP11382321.5*.

Colebrook CF (1939). Turbulent flow in pipes with particular reference to the transition region between the smooth- and rough-pipe laws. *J. Inst. Civil Eng*. **11**:133–156.

Dentz M, Tartakovsky DM (2009). Abrupt-interface solution for carbon dioxide injection into porous media. *Transport In Porous Media*, **79**:15–27.

Estublier A, Lackner AS (2009). Long-term simulation of the Snøhvit CO_2 storage. *Energy Procedia*, 1:3221-3228.

Faust CR, Mercer JW (1979). Geothermal reservoir simulation. 1. Mathematical models for liquid – and vapour – dominated hydrothermal systems. *Water Resources Research*, **15 (1)**:23-30.

Ferronato M, Gambolati G, Janna C, Teatini P (2010). Geomechanical issues of anthropogenic CO_2 sequestration in exploited gas fields. *Energy Conversion Management*, **51**: 1918–1928.

Garcia JE (2003). Fluid Dynamics of Carbon Dioxide Disposal into Saline Aquifers. PhD thesis, University of California, Berkeley.

Ghassemi A, Tarasovs S, Cheng AH-D (2007). A 3-D study of the effects of thermomechanical loads on fracture slip in enhanced geothermal reservoirs. *International Journal of Rock Mechanics and Mining Sciences*, **44**: 1132-1148.

Goerke U-J, Park C-H, Wang W, Singh AK, Kolditz O (2011). Numerical simulation of multiphase hydromechanical processes induced by CO_2 injection into deep saline aquifers. *Oil & Gas Science and Technology*, **66**: 105-118.

Guglielmi Y, Cappa F, Amitrano D (2008). High-definition analysis of fluid-induced seismicity related to the mesoscale hydromechanical properties of a fault zone. *Geophysical Research Letters*, **35**, L06306, doi:10.1029/2007GL033087.

Han WS, Stillman GA, Lu M, Lu C, McPherson BJ, Park E (2010). Evaluation of potential nonisothermal processes and heat transport during CO_2 sequestration. *Journal of Geophysical Research*, **115**, B07209, doi: 10.1029/2009JB006745.

Hasan AR, Kabir CS (2002). Fluid flow and heat transfer in wellbores. SPE Richardson, Texas.

Hassanzadeh H, Pooladi-Darvish M, Keith DW (2009). Accelerating CO_2 dissolution in saline aquifers for geological storage – mechanistic and sensitivity studies. *Energy & Fuels*, **23**: 3328-3336.

Jain L, Bryant, SL (2011). Optimal design of injection/extraction wells for the surface dissolution CO_2 storage strategy. *Energy Procedia*, **4**: 4299-4306.

Kopp A, Class H, Helmig R (2009). Investigation on CO_2 storage capacity in saline aquifers Part 1. Dimensional analysis of flow processes and reservoir characteristics. *International Journal of Greenhouse Gas Control*, **3**:263-276.

Lu M, Connell LD (2008). Non-isothermal flow of carbon dioxide in injection wells during geological storage. *International Journal of Greenhouse Gas Control*, **2**: 248-258.

Majer EL, Baria R, Stark M, Oates S, Bommer J, Smith B, Asanuma H (2007). Induced seismicity associated with Enhanced Geothermal Systems. *Geothermics*, **36**: 185-222.

Mallikamas W, Rajaram H (2005). On the anisotropy of the aperture correlation and effective transmissivity in fractures generated by sliding between identical self-affine surfaces. *Geophysical Research Letters*, **32**, L11401, doi: 10.1029/2005GL022859.

McCoy ST, Rubin ES (2008). An engineering-economic model of pipeline transport of CO_2 with application to carbon capture and storage. *International Journal of Greenhouse Gas Control*, **2**: 219-229.

McPherson BJOL, Han WS, Cole BS (2008). Two equations of state assembled for basic analysis of multiphase CO_2 flow and in deep sedimentary basin conditions. *Comput. Geosci*. **34**: 427–444.

Moran MJ, Shapiro HN, Boettner DD, Bailey MB (2011). *Fundamentals of engineering thermodynamics*. 7th edition, John Wiley & Sons, Inc, USA.

Nickalls RWD (1993). A new approach to solving the cubic: Cardan's solution revealed. *Math. Gazette*, **77**: 354-359.

Nimtz M, Klatt M, Wiese B, Kühn M, Krautz HJ (2010). Modelling of the CO_2 process – and transport chain in CCS systems – Examination of transport and storage processes. *Chemie der Erde*, **70**: 185-192.

Nordbotten JM, Celia MA, Bachu S (2005). Injection and storage of CO_2 in deep saline aquifers: analytical solution for CO_2 plume evolution during injection. *Transp Porous Media,* **58**:339–360.

Olivella S, Carrera J, Gens A, Alonso EE (1994). Non-isothermal multiphase flow of brine and gas through saline media. *Transport In Porous Media,* **15**: 271–93.

Olivella S, Gens A, Carrera J, Alonso EE (1996). Numerical formulation for a simulator (CODE_BRIGHT) for the coupled analysis of saline media. *Eng. Computations,* **13**: 87–112.

Pan L, Oldenburg CN, Wu Y, Pruess K (2009). Wellbore flow model for carbon dioxide and brine. *Energy Procedia*, **1**: 71-78.

Paterson L, Lu M, Connell LD, Ennis-King J (2008). Numerical modeling of pressure and temperature profiles including phase transitions in carbon dioxide wells. SPE Annual Technical Conference and Exhibition, Denver, 21-24 September 2008.

Phillips WS, Rutledge JT, House LS, Fehler MC, (2002). Induced microearthquake patterns in hydrocarbon and geothermal reservoirs: six case studies. *Pure and Applied Geophysics*, **159**: 345–369.

Preisig M, Prévost JH (2011). Coupled multi-phasse thermo-poromechanical effects. Case study: CO_2 injection at In Salah, Algeria. *International Journal of Greenhouse Gas Control*, **5 (4)**: 1055-1064.

Pruess K, Garcia J (2002). Multiphase flow dynamics during CO_2 disposal into saline aquifers. *Environ. Geol*. **42**: 282–295.

Rayward-Smith WJ, Woods AW (2011). Some implications of cold CO_2 injection into deep saline aquifers. *Geophys. Res. Lett.* **38**, L06407, doi:10.1029/2010GL046412.

Redlich O, Kwong JNS (1949). On the thermodynamics of solutions. V. An equation of state. Fugacities of gaseous solutions. *Chem. Rev*. **44**: 233-244.

Rutqvist J, Birkholzer JT, Cappa F, Tsang C-F (2007). Estimating maximum sustainable injection pressure during geological sequestration of CO_2 using coupled fluid flow and geomechanical fault-slip analysis. *Energy Conversion Management*, **48**: 1798–1807.

Rutqvist J, Birkholzer JT, Tsang C-F (2008). Coupled reservoir-geomechanical analysis of the potential for tensile and shear failure associated with CO_2 injection in multilayered reservoir-caprock systems. *International Journal of Rock Mechanics & Mining Sciences*, **45**: 132-143.

Rutqvist J (2012). The geomechanics of CO_2 storage in deep sedimentary formations. *International Journal of Geotechnical and Geological Engineering*, **30**:525-551.

Segall P, Fitzgerald SD (1998). A note on induced stress changes in hydrocarbon and geothermal reservoirs. *Tectonophysics*, **289**: 117-128.

Silva O, Vilarrasa V, Carrera J. (2011). An efficient injection concept for CO_2 geological storage. *6th Trondheim Carbon, Capture and Sequestration Conference,* 14-16 June, Trondheim, Norway.

Singh AK, Goerke U-J, Kolditz O (2011). Numerical simulation of non-isothermal compositional gas flow: Application to carbon dioxide injection into gas reservoirs. *Energy*, **36**: 3446-3458.

Sovova H, Prochazka J (1993). Calculations of compressed carbon dioxide viscosities. *Ind. Eng. Chem. Res*. **32 (12)**: 3162–3169.

Span R,Wagner W (1996). A new equation of state for carbon dioxide covering the fluid region from the triple-point to 1100 K at pressures up to 88 MPa. *J. Phys. Chem. Ref. Data* **25(6)**: 1509–1596.

Spycher N, Pruess K, Ennis-king J (2003). CO_2-H_2O Mixtures in the Geological Sequestration of CO_2. I. Assessment and calculation of mutual solubilities from 12 to 100°C and up to 600 bar. *Geochim. Cosmochim. Acta*, **67**: 3015-3031.

Tsang C-F, Birkholzer J, Rutqvist J (2008). A comparative review of hydrologic issues involved in geologic storage of CO_2 and injection of liquid waste. *Environmental Geology*, **54**: 1723-1737.

van Genuchten R (1980). A closed-form equation for predicting the hydraulic conductivity of unsaturated soils. *Soil Sci. Soc. Am. J.* **44**: 892–898.

Vilarrasa V, Bolster D, Dentz M, Olivella S, Carrera J (2010a). Effects of CO_2 compressibility on CO_2 storage in deep saline aquifers. *Transport In Porous Media*, **85 (2)**: 619-639.

Vilarrasa V, Bolster D, Olivella S, Carrera J (2010b). Coupled hydromechanical modeling of CO_2 sequestration in deep saline aquifers. *International Journal of Greenhouse Gas Control*, **4 (6)**: 910-919.

Vilarrasa V, Koyama T, Neretnieks I, Jing L (2011a). Shear-induced flow channels in a single rock fracture and their effect on solute transport. *Transport In Porous Media*, **87 (2)**: 503-523.

Vilarrasa V, Olivella S, Carrera J (2011b). Geomechanical stability of the caprock during CO_2 sequestration in deep saline aquifers. *Energy Procedia*, **4**: 5306-5313.

Willhite, GP (1967). Over-all transfer coefficients in steam and hot water injection wells. J. Petrol. Technol. (May), 607–615.

Yeo IW, De Freitas MH, Zimmerman RW (1998). Effect of shear displacement on the aperture and permeability of rock. *International Journal of Rock Mechanics and Mining Sciences*, **35(8)**: 1051–1070.

Zendehboudi S, Khan A, Carlisle S, Leonenko Y (2011). Ex situ dissolution of CO_2: a new engineering methodology based on mass-transfer perspective for enhancement of CO_2 sequestration. *Energy & Fuels*, **25**: 3323-3333.

Zigrang DJ, Sylvester ND (1985). A review of explicit friction factor equations. *J Energy Res Tech* **107(2)**: 280-283.

TABLES

Table 1. Material properties used in the thermo-hydro-mechanical analysis of liquid CO_2 injection.

Property	Aquifer	Seal
Permeability, k (m^2)	10^{-13}	10^{-18}
Relative water permeability, k_{rw}	S_w^3	S_w^6
Relative CO_2 permeability, k_{rc}	S_c^3	S_c^6
Gas entry pressure, p_0 (MPa)	0.02	0.6
van Genuchten m	0.8	0.5
Porosity	0.1	0.01
Young's modulus, E (GPa)	2.5	5.0
Poisson ratio, ν	0.3	0.3
Thermal conductivity, λ (W/m/K)	1.5	1.5
Specific heat capacity, c_p (J/kg/K)	874	874
Thermal expansion coefficient, α_T ($ºC^{-1}$)	10^{-5}	10^{-5}

Table 2. Several CO_2 injection conditions at the wellhead ($Q_{inj} = 1.5$ kg/s, geothermal gradient = 0.033 ºC/m, $R_p = 4.5$ cm, $U_\infty = 10$ W m^{-2} K^{-1}) and their estimated compression energy consumption.

Injection conditions at the wellhead	T, ºC	p, MPa	Energy consumption, kW
Gas-phase	35	6.5	409.6
Near-critical point	31	7.0	368.2

Supercritical phase	40	8.0	361.9
Liquid-phase (high T and p)	25	8.0	154.7
Liquid-phase (low T and p)	5	4.2	83.6

Table 3. Operational conditions and parameters for CO_2 injection in SC and liquid state at industrial scale (1.0 Mt/yr)

Variable or parameter	SC CO_2 injection	Liquid CO_2 injection
p, MPa	7.5	2.7
T, ºC	37.0	-10.0
R_p, cm	4.5	7.62
U_∞, W m^{-2} K^{-1}	300	125

FIGURES

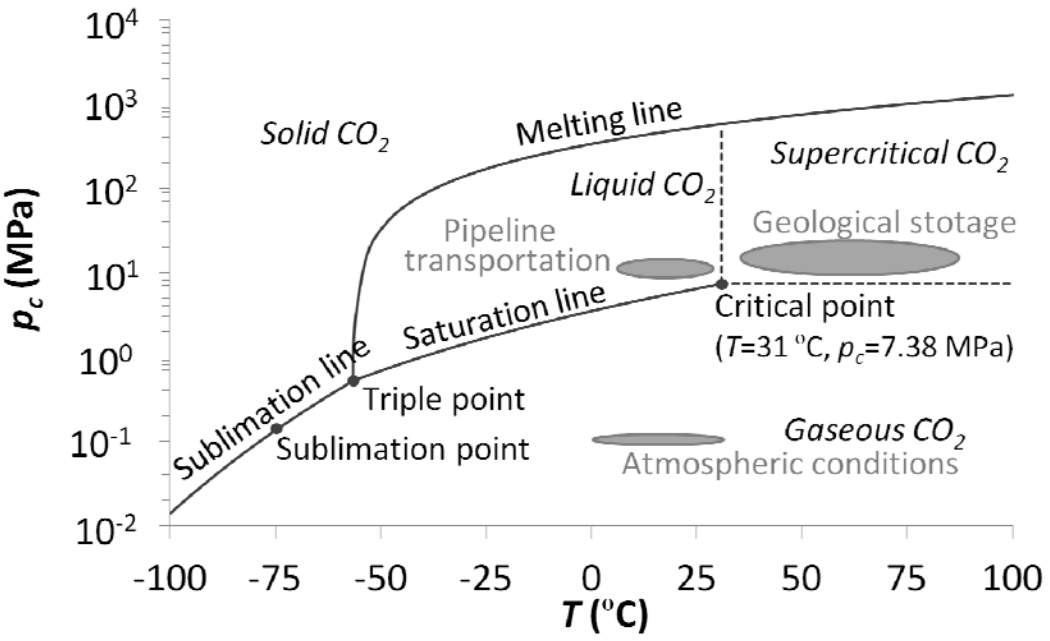

Figure 1. CO_2 phase diagram. CO_2 is a gas in the atmosphere. Pipeline transportation is done in liquid CO_2 conditions and geological storage stays in supercritical CO_2 conditions.

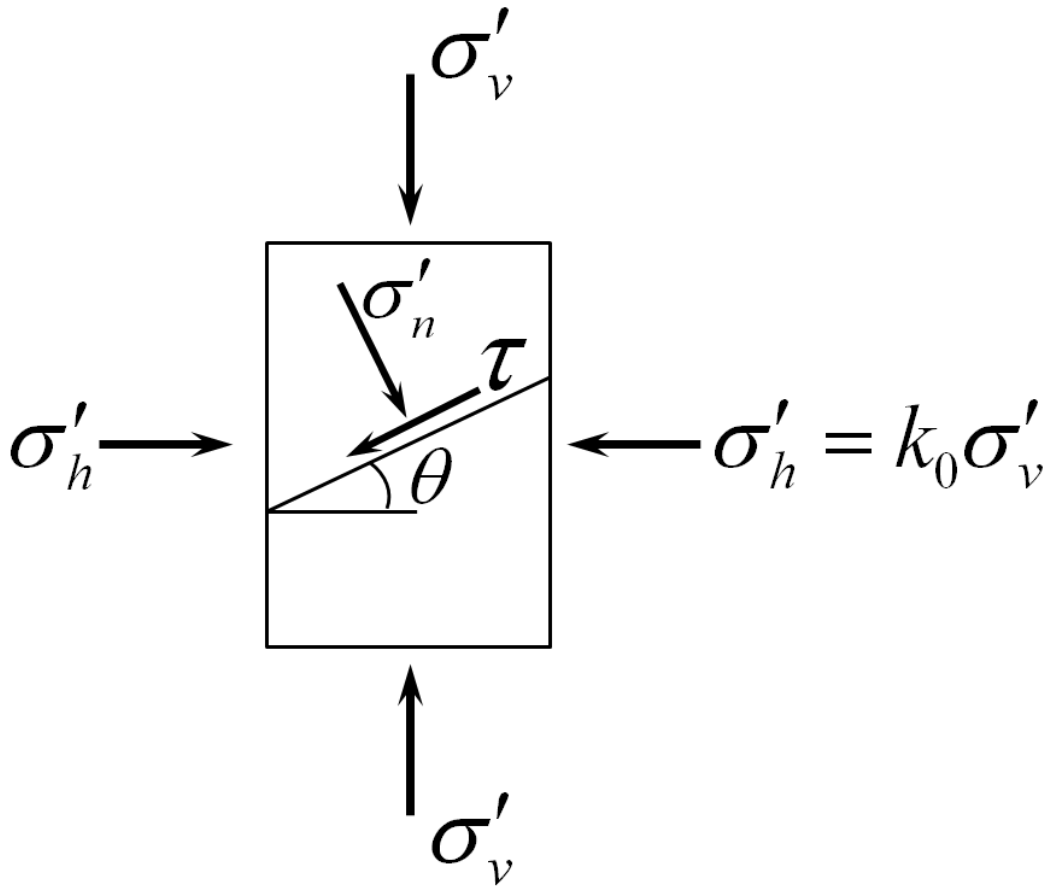

Figure 2. An arbitrary preexisting fracture in a porous media under an axisymmetric stress state.

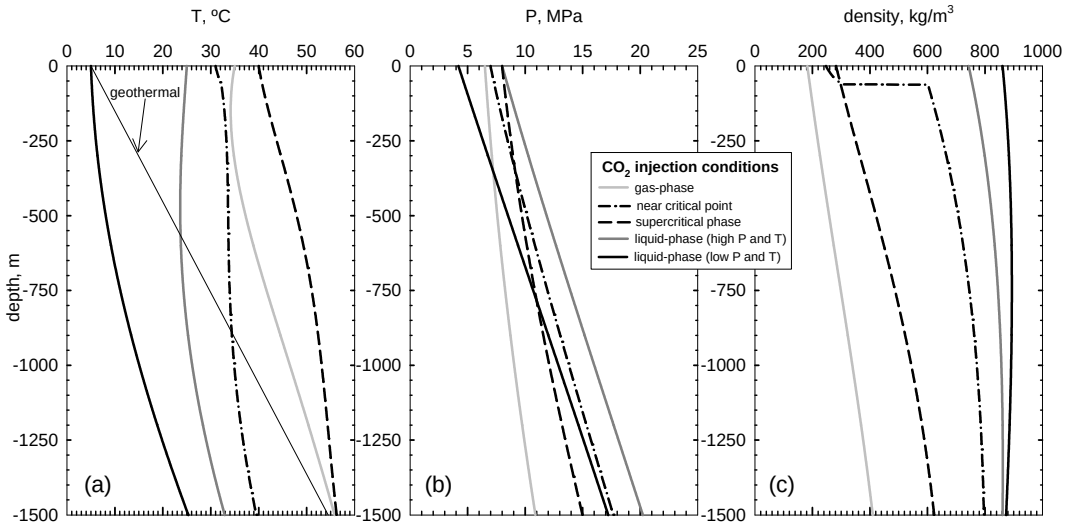

Figure 3. Non-isothermal flow of CO_2 through an injection well: temperature (a), pressure (b) and density (c) profiles. Comparison between different injection conditions at the wellhead (gas-, supercritical- and liquid-phase) ($Q_{inj} = 1.5$ kg/s, geothermal gradient = 0.033 ºC/m, $R_p = 4.5$ cm, $U_\infty = 10$ W m^{-2} K^{-1}).

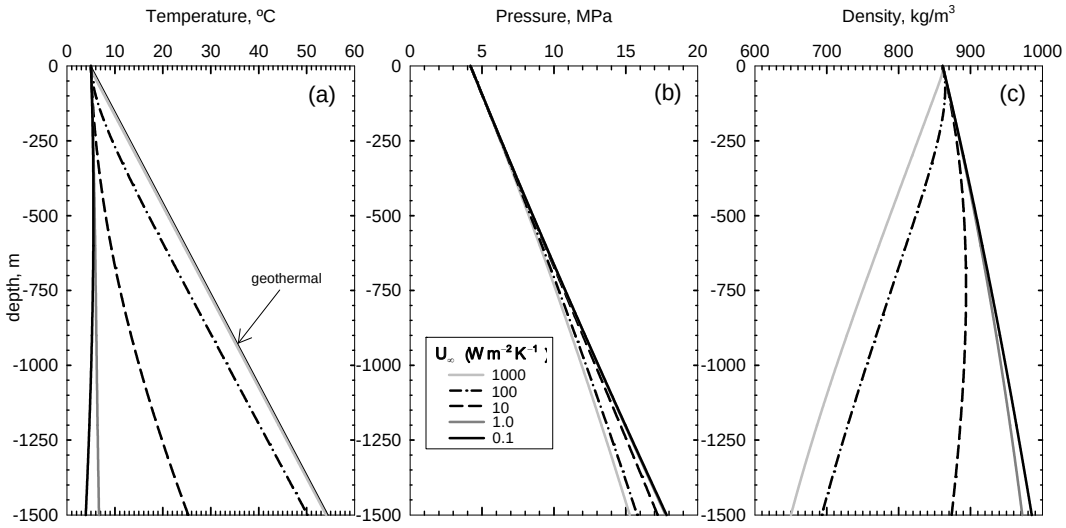

Figure 4. CO_2 injection in liquid-phase at the wellhead. Sensitivity analysis to the overall heat transfer coefficient U_∞. Temperature (a), pressure (b) and density (c) profiles. ($Q_{inj} = 1.5$ kg/s, geothermal gradient = 0.033 ºC/m, $R_p = 4.5$ cm, $T_{inj} = 5.0$ ºC, $p_{inj} = 4.2$ MPa).

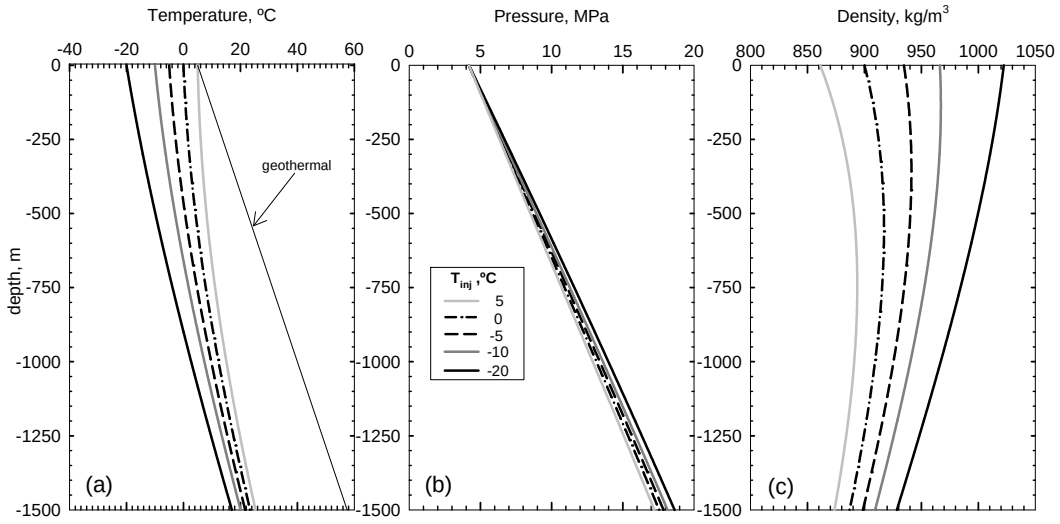

Figure 5. Effect of injection temperature on liquid-phase CO_2 injection. Distributions of temperature (a), pressure (b) and density (c).

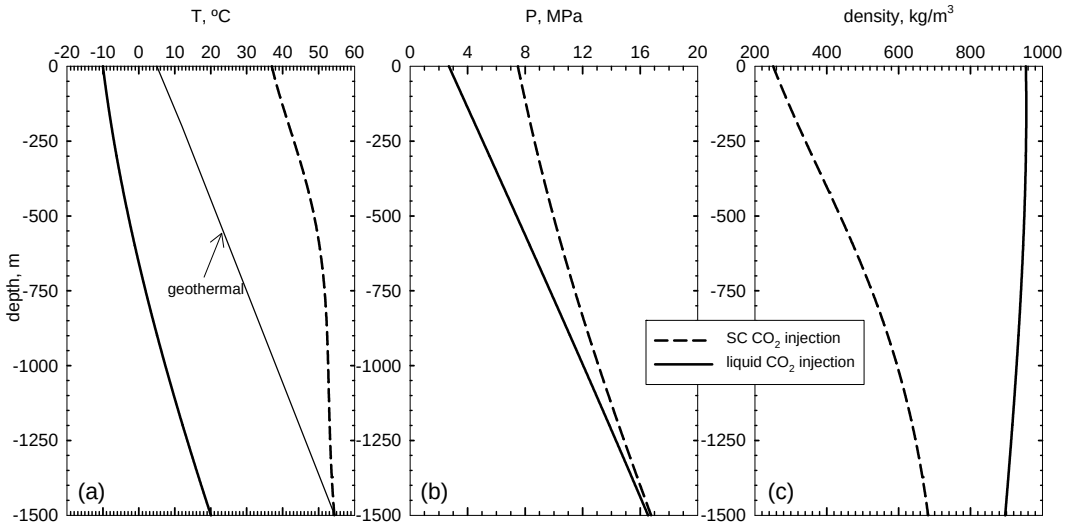

Figure 6. Comparison between SC CO_2 injection (dashed line) and liquid CO_2 injection at industrial scale (1.0 Mt CO_2/yr). Distributions of temperature (a), pressure (b) and density (c).

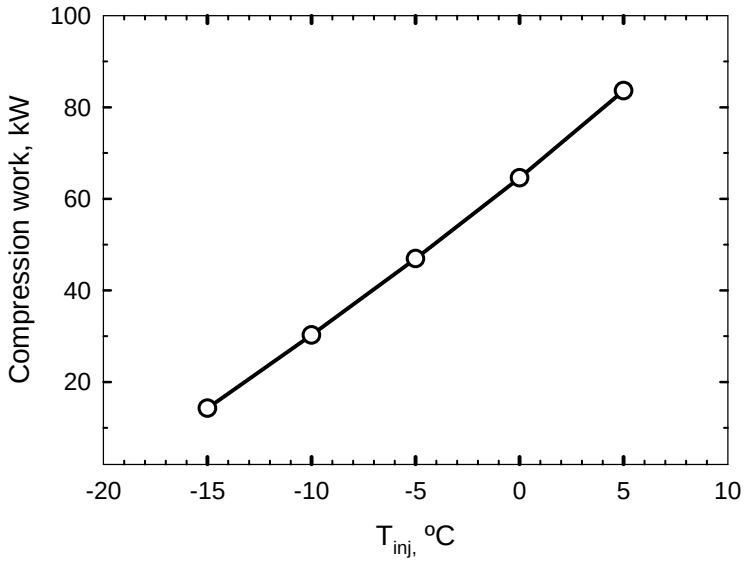

Figure 7. Energy consumption to get the temperature of injection T_{inj} for CO_2 injection in liquid-phase ($Q_{inj} = 1.5$ kg/s, $p_{inj} = 4.2$ MPa) when CO_2 is stored in vessels at -20 ºC and 2.0 MPa.

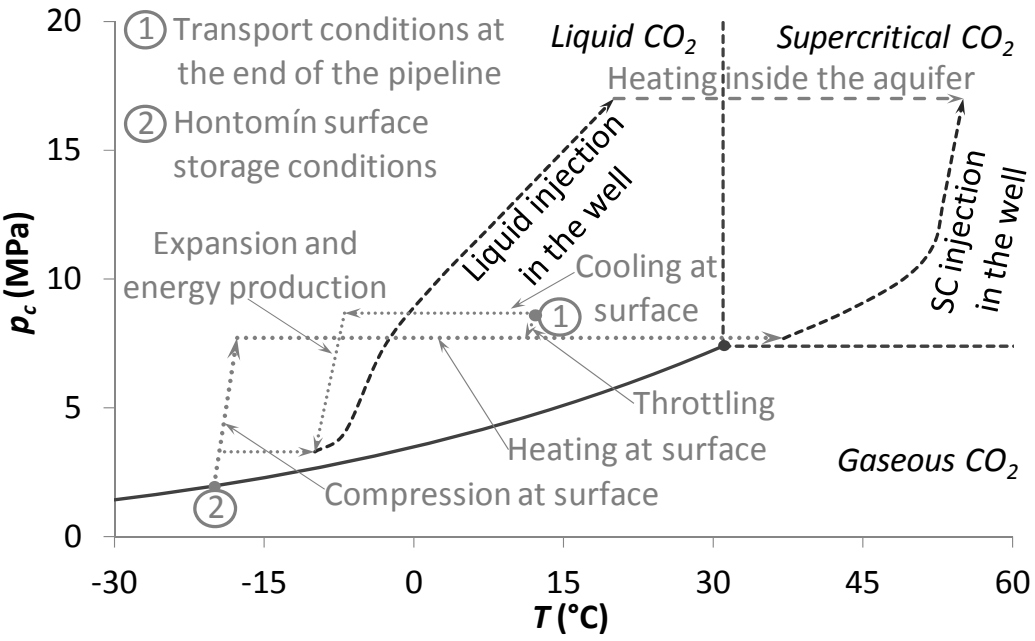

Figure 8. CO_2 diagram with the pressure-temperature trajectories of the surface operations, in the injection well and inside the aquifer for the Hontomín surface storage conditions and for a hypothetical CO_2 transportation in a pipeline at industrial scale with an injection rate of 1 Mt/yr.

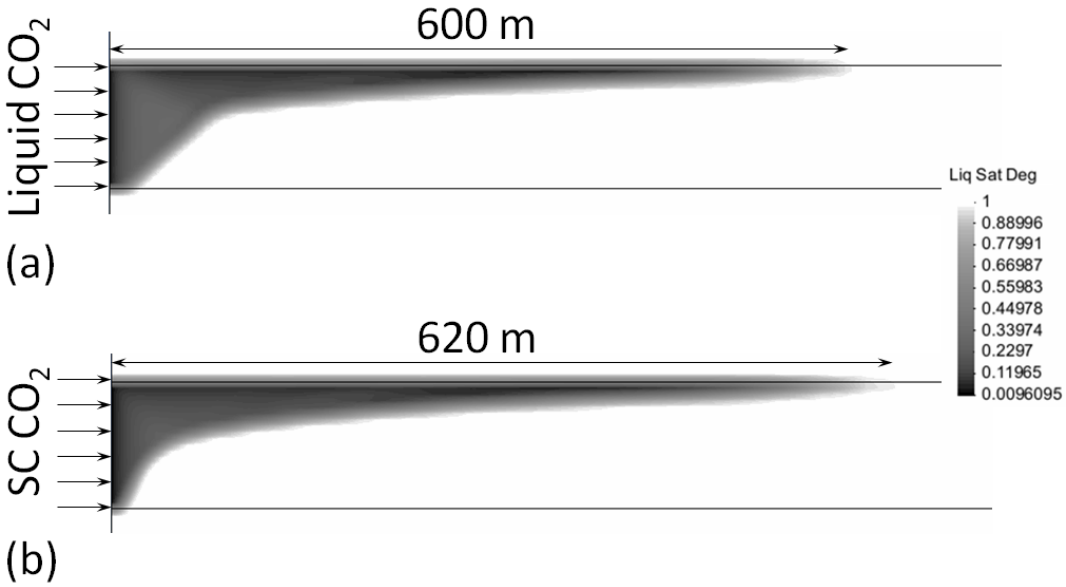

Figure 9. CO_2 plume after 1 year of injecting 1 Mt/yr of CO_2 in (a) liquid and (b) supercritical state.

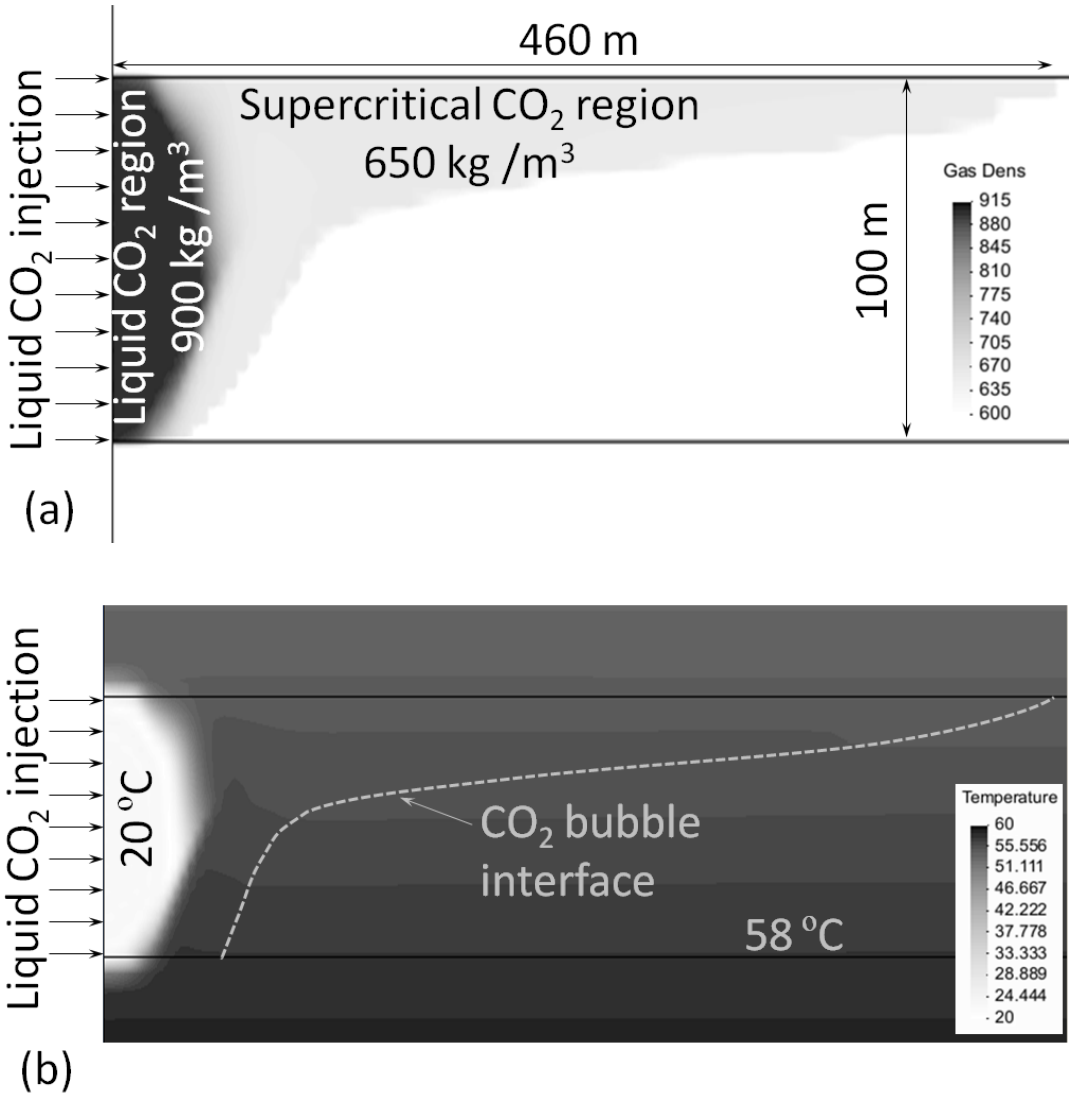

Figure 10. (a) CO_2 density and (b) temperature after 8 months of liquid CO_2 injection. CO_2 remains in liquid state close to the injection well, leading to a steep front because viscous forces dominate gravity forces. Once the CO_2 thermally equilibrates with the medium (in a sharp front), CO_2 stays in SC state, leading to a CO_2 plume interface dominated by gravity forces.

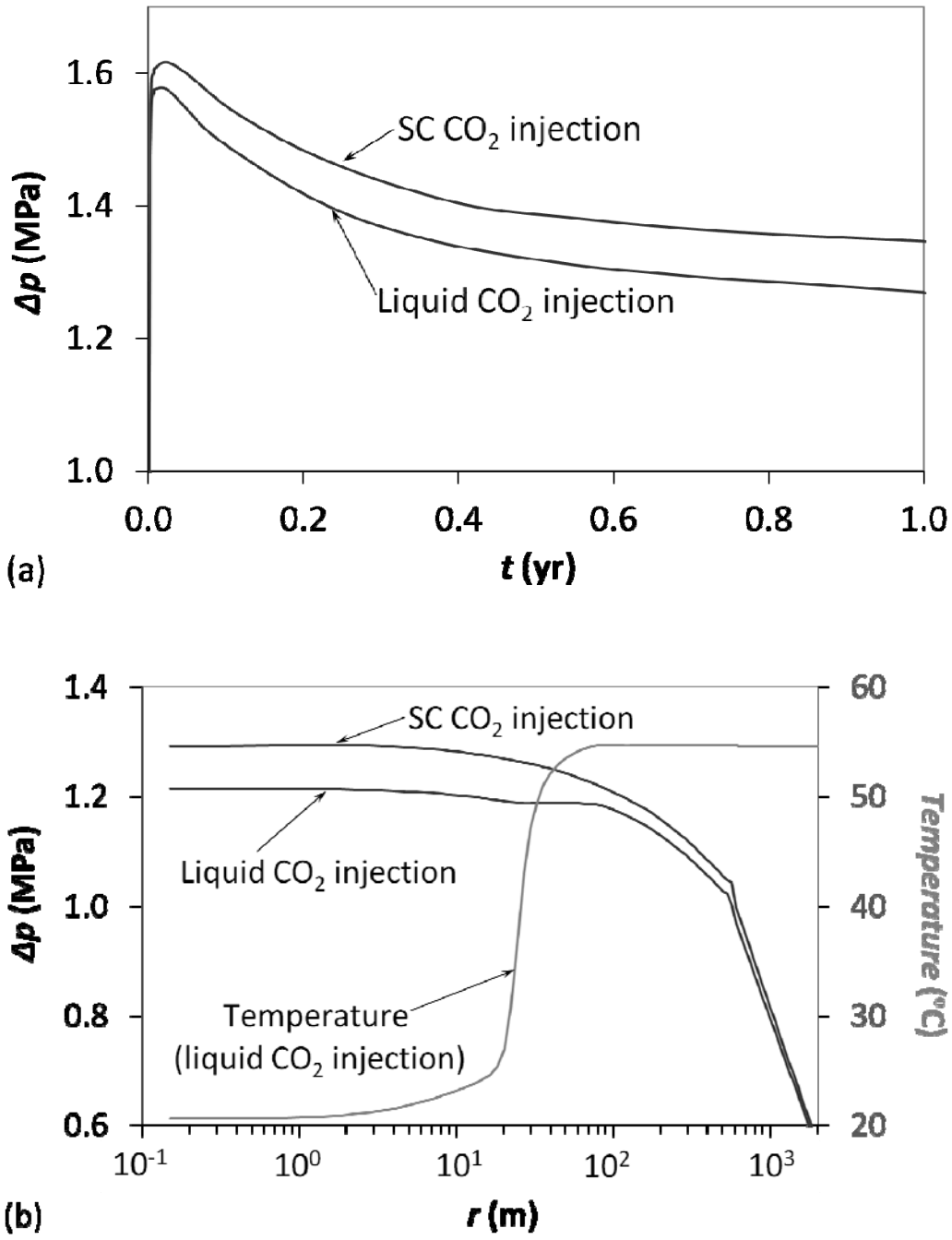

Figure 11. (a) Overpressure evolution at the top of the aquifer in the injection well for liquid and SC CO_2 injection and (b) fluid pressure at the top of the aquifer as a function of radial distance from the injection well after 1 yr of injection.

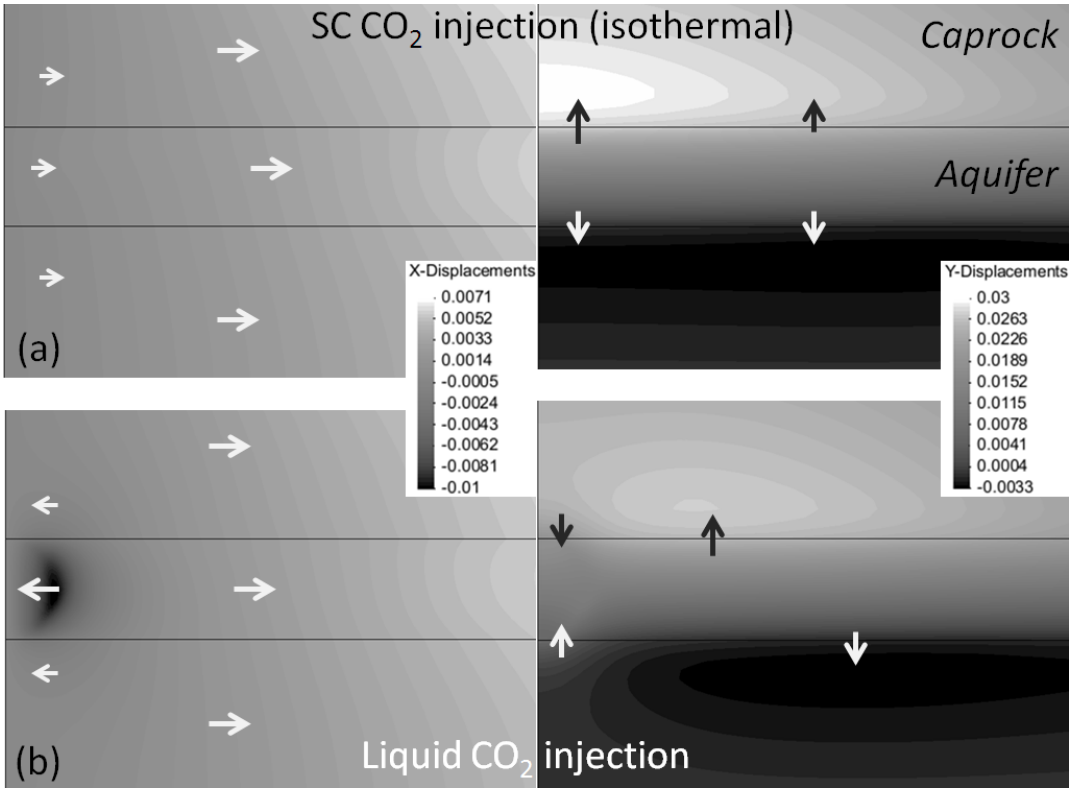

Figure 12. Horizontal and vertical displacements of (a) supercritical and (b) liquid CO_2 injection. Fluid injection pushes the formation laterally and expands it vertically. When injecting cold CO_2, the thermal contraction of the rock is superimposed to the hydraulic effect. The arrows indicate the direction of the displacement.

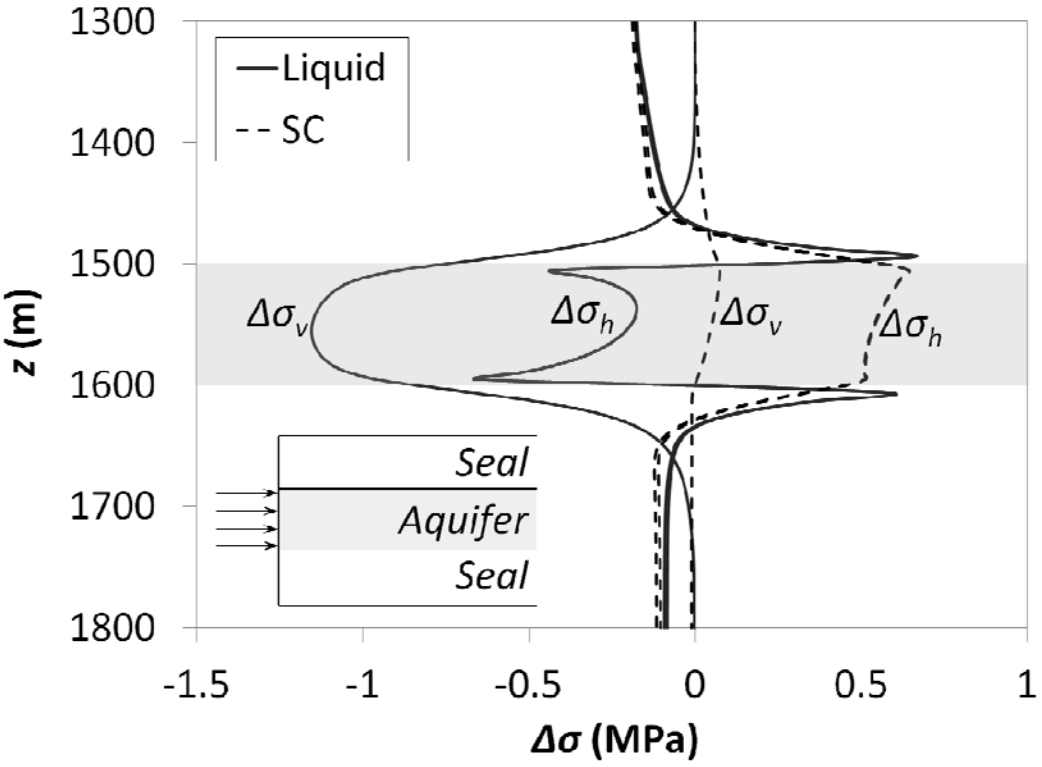

Figure 13. Changes in total stress as a function of depth 3 m away from the injection well for liquid and SC CO_2 injection after 8 months of injection.

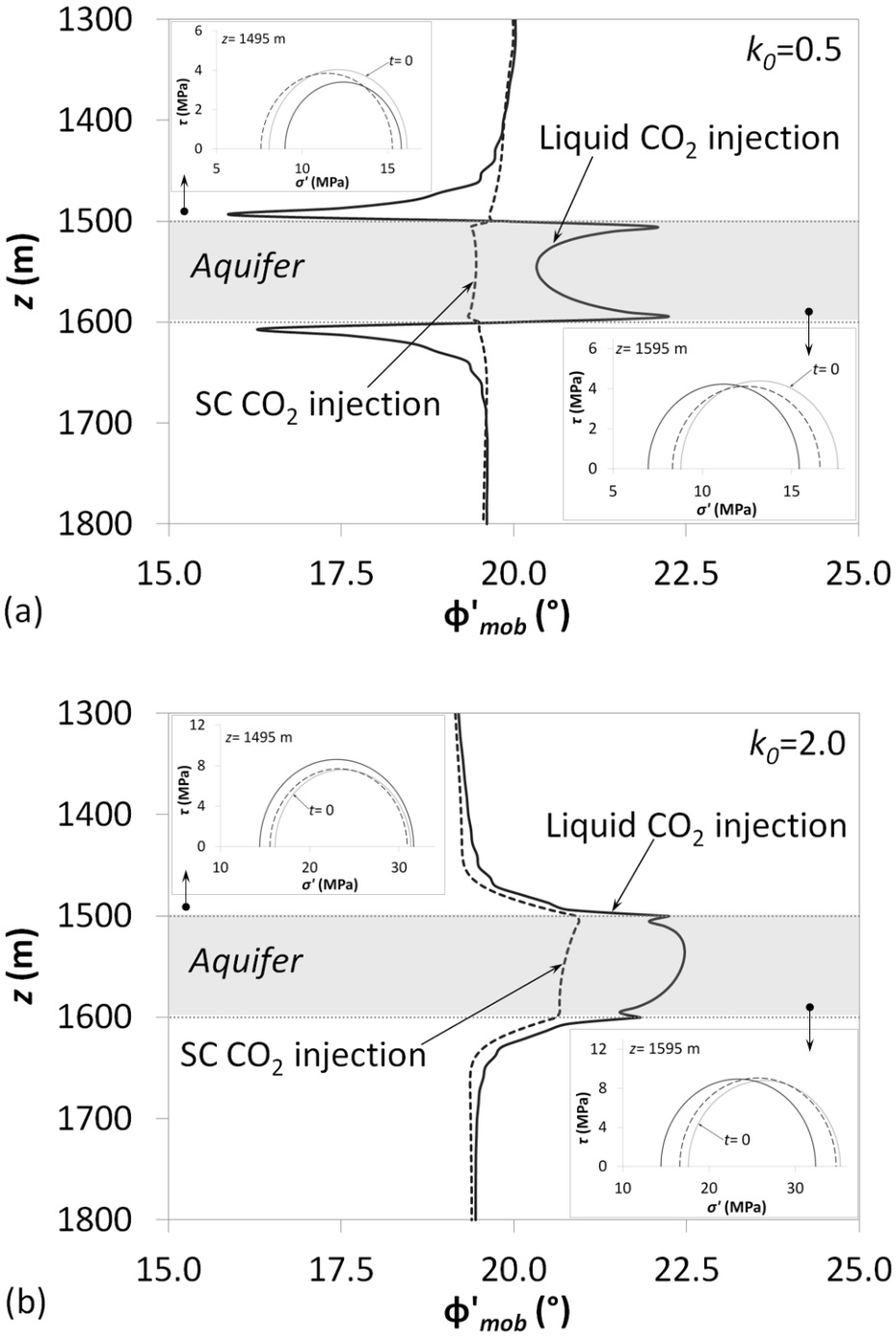

Figure 14. Mobilized friction angle along the vertical for liquid and SC CO_2 injection 3 m away from the injection well after 8 months of injection for a lateral earth pressure coefficient of (a) 0.5 and (b) 2.0. The Mohr circles at depths 1495 m (caprock) and 1595 m (aquifer) are included.

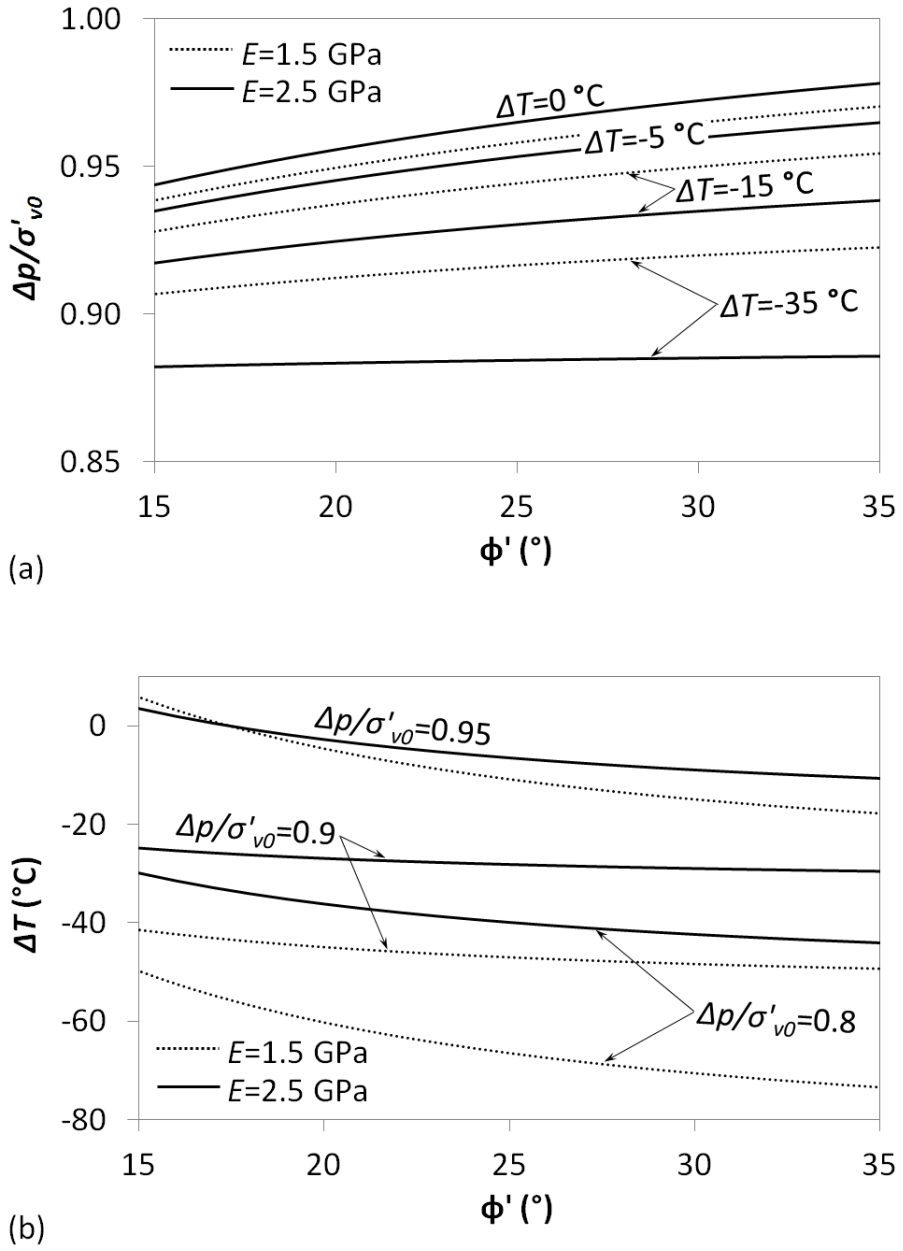

Figure 15. (a) Overpressure normalized by the effective lithostatic stress and (b) temperature drop that is needed to induce a microseismic event at the top of an aquifer placed at 1500 m depth when injecting CO_2 at several temperatures and overpressures, respectively, as a function of the friction angle for a lateral earth pressure coefficient of 0.5 and a Poisson ratio of 0.3 given by Eq. (14) and (15) respectively.